

Non-local Eddy-Mean Kinetic Energy Transfers in Submesoscale-Permitting Ensemble Simulations

Quentin Jamet¹, Stephanie leroux.ste@gmail.com¹, William K. wdewar@fsu.edu²,
thierry.penduff@cnrs.fr Penduff¹, julien.lesommer@univ-grenoble-alpes.fr Le Sommer¹,
Jean-Marc.Molines@univ-grenoble-alpes.fr Molines¹, and jonathan.gula@univ-brest.fr Gula³

¹Institut des Géosciences de l'Environnement

²Florida State University

³Université de Bretagne Occidentale

November 24, 2022

Abstract

Understanding processes associated with eddy-mean flow interactions helps our interpretation of ocean energetics, and guides the development of parameterizations. Here, we focus on the non-local nature of Kinetic Energy (KE) transfers between mean and turbulent reservoirs. Transfers are interpreted as non-local when the energy extraction from the mean flow does not locally sustain energy production of the turbulent flow, or vice versa. The novelty of our approach is to use ensemble statistics to define the mean and the turbulent flow. Based on KE budget considerations, we first rationalize the eddy-mean separation in the ensemble framework, and discuss the interpretation of a mean flow driven by the prescribed (surface and boundary) forcing and a turbulent flow u' driven by non-linear dynamics sensitive to initial conditions. We then analyze 120-day long, 20-member ensemble simulations of the Western Mediterranean basin run at 1/60 resolution. Our main contribution is to recognize the prominent contribution of the cross energy term $\overline{u \cdot h'}$ to explain non-local energy transfers. This provides a strong constraint on the horizontal organization of eddy-mean flow KE transfers since this term vanishes identically for perturbations (u, h') orthogonal to the mean flow (\bar{u}, \bar{h}) . We also highlight the prominent contribution of vertical turbulent fluxes for energy transfers within the surface mixed layer. Analyzing the scale dependence of these non-local energy transfers supports the local approximation usually made in the development of meso-scale, energy-aware parameterizations for non-eddy models, but points out to the necessity of accounting for these non-local effects in the meso-to-submeso scale range.

Non-local Eddy-Mean Kinetic Energy Transfers in Submesoscale-Permitting Ensemble Simulations

Quentin Jamet^{1*}, Stephanie Leroux^{1,2}, William K. Dewar^{1,3}, Thierry Penduff¹,
Julien Le Sommer¹, Jean-Marc Molines¹, Jonathan Gula^{4,5}

¹Univ. Grenoble Alpes, CNRS, IRD, Grenoble INP, IGE, Grenoble, France

²Ocean Next, Grenoble, France

³Dept. of EOAS, Florida State University, Tallahassee, FL, USA

⁴Univ Brest, CNRS, Ifremer, IRD, Laboratoire d'Océanographie Physique et Spatiale (LOPS), IUEM,
Plouzané, France

⁵Institut Universitaire de France (IUF), Paris, France

Key Points:

- Ensemble-based eddy-mean decomposition of kinetic energy budget supports the view of an ocean turbulence driven by internal dynamics
- Turbulent fluxes of the cross-energy term provide a potentially strong horizontal constraint on eddy-mean flow interactions
- Non-localities are leading order at small scales and should be accounted for in meso-to-submeso scale range parameterizations

*Univ. Grenoble Alpes, CNRS, IRD, Grenoble INP, IGE, Grenoble, France

Corresponding author: Quentin Jamet, quentin.jamet@univ-grenoble-alpes.fr

18 **Abstract**

19 Understanding processes associated with eddy-mean flow interactions helps our inter-
 20 pretation of ocean energetics, and guides the development of parameterizations. Here,
 21 we focus on the non-local nature of Kinetic Energy (KE) transfers between mean and
 22 turbulent reservoirs. Transfers are interpreted as non-local when the energy extraction
 23 from the mean flow does not locally sustain energy production of the turbulent flow, or
 24 vice versa. The novelty of our approach is to use ensemble statistics to define the mean
 25 and the turbulent flow. Based on KE budget considerations, we first rationalize the eddy-
 26 mean separation in the ensemble framework, and discuss the interpretation of a mean
 27 flow $\langle \mathbf{u} \rangle$ driven by the prescribed (surface and boundary) forcing and a turbulent flow
 28 \mathbf{u}' driven by non-linear dynamics sensitive to initial conditions. We then analyze 120-
 29 day long, 20-member ensemble simulations of the Western Mediterranean basin run at
 30 $\frac{1}{60}^\circ$ resolution. Our main contribution is to recognize the prominent contribution of the
 31 cross energy term $\langle \mathbf{u}_h \rangle \cdot \mathbf{u}'_h$ to explain non-local energy transfers. This provides a strong
 32 constraint on the horizontal organization of eddy-mean flow KE transfers since this term
 33 vanishes identically for perturbations (\mathbf{u}'_h) orthogonal to the mean flow ($\langle \mathbf{u}_h \rangle$). We also
 34 highlight the prominent contribution of vertical turbulent fluxes for energy transfers within
 35 the surface mixed layer. Analyzing the scale dependence of these non-local energy trans-
 36 fers supports the local approximation usually made in the development of meso-scale,
 37 energy-aware parameterizations for non-eddying models, but points out to the necessity
 38 of accounting for these non-local effects in the meso-to-submeso scale range.

39 **Plain Language Summary**

40 The ocean constantly exchanges energy between its mean and its turbulent reser-
 41 voirs. However, we are still lacking a clear understanding of these eddy-mean flow in-
 42 teractions, which limits our ability to represent them in numerical ocean simulations that
 43 require turbulent closures. Here, we focus on the spatial non-locality of these interac-
 44 tions. We analyze for this the kinetic energy exchanges between the ensemble mean and
 45 the residual flow during the decorrelation phase of an ensemble of submesoscale-permitting
 46 simulations of the Western Mediterranean basin. Our main contribution is to highlight
 47 the prominent role played by turbulent fluxes of the cross-energy term $\langle \mathbf{u}_h \rangle \cdot \mathbf{u}'_h$ in driv-
 48 ing non-local kinetic energy transfers. Through these turbulent fluxes, the energy lost
 49 by the ensemble mean flow at one location can be transported over tens of kilometers

50 before to be transferred to the turbulent flow (or vice versa), making the eddy-mean ki-
 51 netic energy transfers non-local. We then analyze the geographical organization of these
 52 turbulent fluxes, and highlight a potentially strong horizontal constraint on eddy-mean
 53 flow interactions owing to their particular dynamics. Finally, we quantify the scale de-
 54 pendence of these non-localities, and suggest that their effects should be accounted for
 55 in meso-to-submeso scale range parameterizations.

56 **1 Introduction**

57 Meso-scale eddies play a crucial role for the energetic balance of the ocean, providing
 58 the main pathway toward dissipative scales (Wunsch & Ferrari, 2004). Understanding
 59 how these eddies interact with the mean flow thus helps our interpretation of the ocean
 60 circulation, and also serves as a basis for the development of robust parameterizations
 61 for ocean models. In order to gain insights from the different processes controlling the
 62 energetic of these eddies, it is usual and natural to investigate the different terms con-
 63 tributing to the time rate of change of the Eddy Kinetic Energy (EKE) equation (e.g.,
 64 Webster, 1961, 1965; Dewar & Bane, 1989). From a point of view of parameterization,
 65 evaluating the energy levels of meso-scale 'eddies' is used to constrain numerical eddy
 66 dissipation coefficients through mixing length arguments (Cessi, 2008; Eden & Great-
 67 batch, 2008; Mak et al., 2018; Jansen et al., 2019), thus making these coefficients energy-
 68 aware. In this context, the 'eddies' are associated with unresolved, sub-grid scale physics
 69 that need to be parameterized. Processes controlling this physics thus need to be rep-
 70 resented based on the *mean*, resolved flow. A particularity of eddy-mean kinetic energy
 71 transfers lies in the difference in the terms involved in KE budget of the mean and the
 72 turbulent flow. That is, changes in the energy of the mean flow are subject to the diver-
 73 gence of an eddy stress tensor correlated with the mean flow, while changes in the en-
 74 ergy of the turbulent flow are subject to a turbulent flux up or down the gradient of the
 75 mean flow. Equating the eddy-mean interaction term from these two different perspec-
 76 tives is subject to an assumption of locality, where the energy released by the mean flow
 77 at one location is assumed to sustain the growth of eddies at that location (or vice versa
 78 for energy backscattering processes). However, recent studies based on Lorenz energy
 79 cycles at global (Chen et al., 2014, 2016) and regional (Kang & Curchitser, 2015; Capó
 80 et al., 2019) scales have shed light on the strong non-locality of these transfers at small
 81 scales. Our interest in this study is to further investigate the non-local nature of these

82 eddy-mean kinetic energy transfers, leveraging the recent developments of kilometric-
83 scale resolution ensemble simulations to separate mean and eddies based on ensemble
84 statistics.

85 An emerging concern for the development of turbulent parameterizations for ocean
86 models is placed on the non-locality of energy transfers. In early work on energy-aware
87 parameterizations for mesoscale turbulence, Cessi (2008) has proposed an improved Gent-
88 McWilliams (Gent & McWilliams, 1990) formulation in which the eddy buoyancy dif-
89 fusivity was defined as a function of the averaged sub-grid scale turbulent kinetic energy
90 through mixing length arguments. Although globally integrated estimates of sub-grid
91 scale kinetic energy offer interesting properties (Marshall & Adcroft, 2010), it obviously
92 *only* provides an averaged estimate. Other studies have provided more elaborated for-
93 mulations to account for the spatial organization of mesoscale eddy diffusivity (Visbeck
94 et al., 1997; Ferreira et al., 2005; Groeskamp et al., 2020), but at the expense of severely
95 complicating the prognostic equation of sub-grid scale turbulent kinetic energy that needs
96 to be solved (Eden & Greatbatch, 2008; Mak et al., 2018; Jansen et al., 2019). In prac-
97 tice, the several processes involved in this prognostic equation are usually parameterized
98 through isotropic dissipative operators, mostly due to the lack of better theories. How-
99 ever, Grooms (2017) has recently shown that, while this approximation is valid for isotropic
100 barotropic turbulence with no mean flow, idealized advection-diffusion models rapidly
101 fail to accurately represent the transport of EKE when a mean flow is added to the prob-
102 lem (through the β effect in his case). A potential reason to explain this is associated
103 with the non-locality of the eddy energy transfers, as for instance identified in a wind-
104 driven, two-layer QG model by Grooms et al. (2013); in this simulation, the energy lost
105 by eddies in the separated jet is primarily balanced by imports of energy from remote
106 regions. Non-local kinetic energy reported by Grooms et al. (2013) are associated with
107 various processes, such as wave radiation, advection, or eddy-mean flow interactions. The
108 latter relates the dynamics behind energy transfers between the mean and the turbulent
109 flow. The leading order contribution of this latter term has been recently reported by
110 Chen et al. (2014), Kang and Curchitser (2015) and Capó et al. (2019) in realistic sim-
111 ulations, and is thus likely to have important implications for the development of future
112 parameterizations.

113 There are many ways to define 'mean' and 'eddies', the most traditional approach
114 being to use a time averaging. This definition offers several advantages, such as ease in

115 implementation and natural interpretation when dealing with observations. Eddies so
 116 defined are however associated with all signals that vary in time, which makes the at-
 117 tribution of processes somehow ambiguous (for instance to disentangle processes asso-
 118 ciated with hydrodynamic instabilities from those associated with time varying forcing).
 119 Coarse-graining (e.g. Aluie et al., 2018) offers an alternative approach, which is more
 120 intuitive in the context of parameterization. Although the time dimension is retained,
 121 this approach induces some subjectivity in the definition of length scale cutoff, thus the
 122 size of the eddies, as well as complexities in dealing with solid boundaries, isotropy and
 123 inhomogeneities of the flow structure.

124 Here, we choose to leverage ensemble simulations to define the 'mean' flow as that
 125 common to all members (i.e. an ensemble mean), and the 'eddies' as the deviation of each
 126 member with its ensemble mean. We will argue in the following that this approach of-
 127 fers an unambiguous definition of 'eddies' through KE budget considerations; it allows
 128 to robustly separate the flow in a part that is controlled by the prescribed forcing (the
 129 'mean' flow), and a part that is intrinsically driven by non-linear dynamics (the 'eddies').
 130 This strategy also allows the analysis of the spatio-temporal structure of ocean turbu-
 131 lence and its associated flux of energy. An obvious limitation is associated with the com-
 132 putational resources required to produce such a data set. Here, in order to partially ac-
 133 count for the potential effects of submesoscale dynamics in eddy-mean flow interactions,
 134 we have used the newly generated kilometric-scale resolution ($\frac{1}{60}^\circ$) MEDWEST60 en-
 135 semble simulations of Leroux et al. (2021). It is composed of 20 ensemble members sub-
 136 ject to small initial conditions uncertainties (usually referred to as *micro* initial condi-
 137 tions ; Stainforth et al., 2007), run for 120-days from the already spun-up oceanic state
 138 of eNATL60 simulation (Brodeau et al., 2020), a numerically identical, single simulation
 139 run over the whole North Atlantic basin. Analyzing the decorrelation of each ensemble
 140 member in this context informs us on the processes controlling the growth of ensemble
 141 spread, thus on the spatio-temporal structure of eddy-mean flow interactions.

142 The paper is organized as follows. In Section 2, we present the MEDWEST60 en-
 143 semble simulations, along with the associated mean and eddy kinetic energy budget de-
 144 composition. We then discuss the decorrelation of the turbulent flow from initial con-
 145 ditions, and some aspects of the associated kinetic energy budgets in Section 3. In Sec-
 146 tion 4, we first diagnose the non-local kinetic energy transfers, and then estimate the scale

147 dependence of these processes with a view toward parameterization. We finally summa-
 148 rize our results and discuss their implications in Section 5.

149 2 Methods

150 2.1 Kinetic Energy Budget of Ensemble Simulations

151 Our primary interest is to investigate the kinetic energy budget of the MEDWEST60
 152 submesoscale-permitting ensemble simulations, described in Section 2.2, with a focus on
 153 energy transfers between the ensemble mean and the turbulent flow. The momentum equa-
 154 tions solved by these simulations are the Boussinesq, hydrostatic equations written in
 155 flux form:

$$\partial_t u = -\nabla \cdot \mathbf{u}u + fv - \frac{1}{\rho_0} \partial_x p + \mathbf{D}_u, \quad (1a)$$

$$\partial_t v = -\nabla \cdot \mathbf{u}v - fu - \frac{1}{\rho_0} \partial_y p + \mathbf{D}_v, \quad (1b)$$

156 with $\mathbf{u} = (u, v, w)$ the three-dimensional velocity field, $\nabla = (\partial_x, \partial_y, \partial_z)$ the three-dimensional
 157 gradient, $f = 2\Omega \sin(\phi)$ the Coriolis frequency, $p = \int_z^\eta \rho g dz$ the (hydrostatic and sur-
 158 face) pressure field, and $\mathbf{D}_u = \partial_z (\mathbf{A} \partial_z u)$ and $\mathbf{D}_v = \partial_z (\mathbf{A} \partial_z v)$, the viscous effects in-
 159 cluding both surface wind forcing and bottom drag as upper and bottom boundary con-
 160 ditions, respectively, as well as interior ocean dissipation of momentum, with \mathbf{A} the spatio-
 161 temporally varying viscous coefficient computed through the TKE turbulent closure scheme¹.
 162 Following standard practices, an equation for the hydrostatic kinetic energy

$$K = \frac{\rho_0}{2} (\mathbf{u}_h \cdot \mathbf{u}_h), \quad (2)$$

163 with $\mathbf{u}_h = (u, v)$ the horizontal component of the velocity field, is obtained by multi-
 164 plying (1a) by $\rho_0 u$ and (1b) by $\rho_0 v$, and summing the resulting equations, such that:

$$\partial_t K = -\nabla \cdot \mathbf{u}K - \mathbf{u}_h \cdot \nabla_h p + \rho_0 \partial_z (\mathbf{A} \partial_z K) - \epsilon, \quad (3)$$

165 with $\nabla_h = (\partial_x, \partial_y)$ the horizontal gradient, $\rho_0 \partial_z (\mathbf{A} \partial_z K)$ the work done by vertical vis-
 166 cous forces, and $\epsilon = \rho_0 \mathbf{A} \partial_z \mathbf{u}_h \partial_z \mathbf{u}_h$ the vertical dissipation. Adding and subtracting $-w \partial_z p =$
 167 wb in (3), and using the continuity equation for Boussinesq fluids $\nabla \cdot \mathbf{u} = 0$, allows the

¹ Note that horizontal viscous effects are implicitly included in the UBS advective scheme as a biharmonic operator (Shchepetkin & McWilliams, 2005). See Appendix for further details on these operators and their implementation in MEDWEST60.

168 pressure term to be written as the divergence of a flux, and makes explicit the exchange
 169 of kinetic energy with potential energy through wb . It leads to:

$$\partial_t K = -\nabla \cdot \mathbf{u}K - \nabla \cdot \mathbf{u}p - wb + \rho_0 \partial_z (\mathbf{A} \partial_z K) - \epsilon. \quad (4)$$

170 In our ensemble simulations, the velocity field simulated by each individual ensemble mem-
 171 ber obeys this KE equation. It is however possible, from ensemble statistics, to decom-
 172 pose this velocity field as that common to all members, and that specific to each mem-
 173 ber, and analyze their kinetic energy expression.

174 For this, we consider the Reynolds decomposition

$$x_n = \langle x \rangle + x'_n, \quad (5)$$

175 where the mean operator

$$\langle x \rangle = \frac{1}{N} \sum_{n=1}^N x_n. \quad (6)$$

176 represents the ensemble mean, with N the size of the ensemble. Following this proce-
 177 dure to decompose the zonal and meridional velocities defining the kinetic energy (2) leads
 178 to:

$$K = \tilde{K} + K^* + \rho_0 \langle \mathbf{u}_h \rangle \cdot \mathbf{u}'_h, \quad (7)$$

179 where $\tilde{K} = \frac{\rho_0}{2} (\langle \mathbf{u}_h \rangle \cdot \langle \mathbf{u}_h \rangle)$ and $K^* = \frac{\rho_0}{2} (\mathbf{u}'_h \cdot \mathbf{u}'_h)$. For reasons explained below, we will
 180 refer the former quantity (\tilde{K}) as the Forced Kinetic Energy (FKE), and the ensemble
 181 mean of the latter quantity ($\langle K^* \rangle$) as the Internal Kinetic Energy (IKE). This refers to
 182 the kinetic energy of the ensemble mean flow and that of the perturbations, respectively.
 183 The notation used here is somehow different from the more classical Mean and Eddy Ki-
 184 netic Energy (MKE, EKE) terminology used when working with time averages. While
 185 these terms are formally the same, the different terminology used here aims at highlight-
 186 ing differences in their interpretation and properties in the context of ensemble simula-
 187 tions. Such differences are further discussed in the following. Finally, we note that the
 188 vector form employed here also emphasizes that, in addition to vanishing identically upon
 189 averaging, the cross energy term $\rho_0 \langle \mathbf{u}_h \rangle \cdot \mathbf{u}'_h$ is also zero for turbulent flow orthogonal
 190 to the mean flow.

191 The kinetic energy equation for the mean flow and that for the perturbations are
 192 usually derived based on averaged and residual forms of (1a) and (1b). Formally, mul-
 193 tiplying the ensemble mean equations $\langle (1a) \rangle$ and $\langle (1b) \rangle$ by the ensemble mean zonal and

194 meridional velocities $\rho_0 \langle u \rangle$, $\rho_0 \langle v \rangle$, respectively, and summing the resulting equations,
 195 leads to an equation for the Forced Kinetic Energy (FKE) of the form:

$$\partial_t \tilde{K} = -\nabla \cdot \langle \mathbf{u} \rangle \tilde{K} - \underline{\rho_0 \langle \mathbf{u}_h \rangle \cdot \nabla \cdot \langle \mathbf{u}' \mathbf{u}'_h \rangle} - \nabla \cdot \langle \mathbf{u} \rangle \langle p \rangle - \langle w \rangle \langle b \rangle + \rho_0 \partial_z \left(\langle \mathbf{A} \rangle \partial_z \tilde{K} \right) - \epsilon_{\tilde{K}}, \quad (8)$$

196 where the underlined term is associated with eddy-mean flow interactions, and the ex-
 197 change of FKE with forced potential energy is made explicit through the inclusion of $\langle w \rangle \langle b \rangle$.
 198 A similar equation is obtained for the Internal Kinetic Energy (IKE) by multiplying the
 199 residual equation for the zonal and meridional momentum (1a)' and (1b)' by the zonal
 200 and meridional velocity perturbations $\rho_0 u'$ and $\rho_0 v'$, ensemble averaging and then sum-
 201 ming the resulting equations. This leads to:

$$\partial_t \langle K^* \rangle = -\nabla \cdot \langle \mathbf{u} K^* \rangle - \underline{\rho_0 \langle \mathbf{u}' \mathbf{u}'_h \rangle \cdot \nabla \cdot \langle \mathbf{u}_h \rangle} - \nabla \cdot \langle \mathbf{u}' p' \rangle - \langle w' b' \rangle + \rho_0 \partial_z \langle \mathbf{A}' \partial_z K^* \rangle - \epsilon_{K^*}, \quad (9)$$

202 where the first term on the RHS of (9) includes advection of IKE by both the ensem-
 203 ble mean and the turbulent flow, and the underlined term is associated with eddy-mean
 204 flow interactions. Again, the exchange of IKE with internal potential energy is made ex-
 205 plicit through the inclusion of $\langle w' b' \rangle$. The sum of (8) and (9) leads to an equation for
 206 the ensemble mean kinetic energy of the full flow.

207 Another, yet equivalent, procedure to derive an equation for the ensemble mean
 208 kinetic energy of the full flow consists in expanding the different components of (4) fol-
 209 lowing the Reynolds decomposition in the ensemble dimension (5), then ensemble av-
 210 eraging. This leads to:

$$\begin{aligned} \partial_t \langle K \rangle = & -\nabla \cdot \langle \mathbf{u} \rangle \tilde{K} - \nabla \cdot \langle \mathbf{u} K^* \rangle - \underline{\rho_0 \nabla \cdot \langle \mathbf{u}' (\langle \mathbf{u}_h \rangle \cdot \mathbf{u}'_h) \rangle} \\ & - \nabla \cdot \langle \mathbf{u} \rangle \langle p \rangle - \nabla \cdot \langle \mathbf{u}' p' \rangle - \langle w \rangle \langle b \rangle - \langle w' b' \rangle + \rho_0 \partial_z \left(\langle \mathbf{A} \rangle \partial_z \tilde{K} \right) + \rho_0 \partial_z \langle \mathbf{A}' \partial_z K^* \rangle - \epsilon_{\tilde{K}} - \epsilon_{K^*}, \end{aligned} \quad (10)$$

211 where $\epsilon_{\tilde{K}}$ and ϵ_{K^*} represents dissipation of FKE and IKE, respectively. Here, the un-
 212 derlined term emerged from the advection of the cross energy term $\langle \mathbf{u}_h \rangle \cdot \mathbf{u}'_h$ by the per-
 213 turbations. This reflects that, although this term vanishes identically upon averaging,
 214 its advection by perturbations does not. This is of particular interest because it is as-
 215 sociated with kinetic energy transfers between the mean and the turbulent flow, thus plays
 216 a critical role in eddy-mean flow interactions. Indeed, following the chain rule, this term
 217 can be decomposed as

$$\nabla \cdot \langle \mathbf{u}' (\langle \mathbf{u}_h \rangle \cdot \mathbf{u}'_h) \rangle = \langle \mathbf{u}_h \rangle \cdot \nabla \cdot \langle \mathbf{u}' \mathbf{u}'_h \rangle + \langle \mathbf{u}' \mathbf{u}'_h \rangle \cdot \nabla \langle \mathbf{u}_h \rangle, \quad (11)$$

218 where the continuity equation has been used to express the last term of the RHS of (11)
 219 in a more conventional way. The first term of the RHS of (11) is the covariance of the
 220 horizontal mean flow with the divergence of the Reynolds stress tensor associated with
 221 the FKE equation, and the second term of the RHS of (11) is the eddy momentum fluxes
 222 up or down the gradient of the mean flow associated with the IKE equation. It is then
 223 straightforward to show that expanding the underlined term in (10) as (11) leads to an
 224 equation for the ensemble mean kinetic energy of the full flow that equates the sum of
 225 the FKE and the IKE equation, i.e., Eq. (8) and Eq. (9). In the following, we will re-
 226 fer to the three terms of (11), from left to right, as the DIVergence of Eddy Fluxes (DI-
 227 VEF), the Mean-to-Eddy energy Conversion (MEC), and the EDDY momentum FLuX
 228 (EDDYFLX).

229 By volume integration, several components of (10) become statements about fluxes
 230 at the boundaries of the volume of integration through the divergence theorem. In en-
 231 semble simulations such as those we analyze here, ocean surface and boundary condi-
 232 tions are usually prescribed as ensemble mean conditions, common to all members, such
 233 that we can neglect turbulent fluxes at the (surface and open) boundaries. (This, along
 234 with bottom turbulent fluxes, are further discussed in Section 2.3). Under such assump-
 235 tions, several terms of the integrated version of (10) vanish, and the domain integrated
 236 equation for the ensemble mean kinetic energy of the full flow simplifies to:

$$\begin{aligned} \partial_t \int_V \langle K \rangle dV &= \partial_t \int_V \tilde{K} dV + \partial_t \int_V \langle K^* \rangle dV = \\ &= - \int_S \langle \mathbf{u} \rangle \tilde{K} \cdot \mathbf{n} dS - \int_S \langle \mathbf{u} \rangle \langle p \rangle \cdot \mathbf{n} dS - \int_V (\langle w \rangle \langle b \rangle + \langle w' b' \rangle) dV \\ &\quad + \int_A \langle \mathbf{u}_h \rangle \cdot \langle \boldsymbol{\tau} \rangle dA - \int_B \langle \mathbf{u}_h \rangle \cdot \langle \mathbf{F} \rangle dB - \int_V (\epsilon_{\tilde{K}} + \epsilon_{K^*}) dV, \end{aligned} \quad (12)$$

237 where V is the volume of integration, S the surface bounding V , A and B its ocean sur-
 238 face and bottom part, respectively, and \mathbf{n} the normal to the surface S . Here, the work
 239 done by surface wind stress and bottom friction ($\int_A \langle \mathbf{u}_h \rangle \cdot \langle \boldsymbol{\tau} \rangle dA$ and $\int_B \langle \mathbf{u}_h \rangle \cdot \langle \mathbf{F} \rangle dB$
 240 with \mathbf{F} the vertical diffusive flux at the bottom boundary, respectively) comes from the
 241 volume integration of viscous forces. The time rate of change of kinetic energy within
 242 the domain thus reflects the import/export of FKE and the wave field prescribed at the
 243 open boundaries (two first terms), exchanges with potential energy (third term), work
 244 associated with prescribed surface forcing (fourth term) and bottom boundary condi-
 245 tion (fifth term), and dissipation (last term). We note here that although the transfers
 246 of kinetic energy between the mean and the turbulent flow (underlined term in (10)) can

247 be locally large, they cancel each other when integrated over the entire basin to satisfy
 248 the boundary condition of no turbulent flux of the LHS of (11).

249 The turbulent version of (12) summarizes as:

$$\partial_t \int_V \langle K^* \rangle dV = -\rho_0 \int_V \langle \mathbf{u}' \mathbf{u}'_h \rangle \cdot \nabla \langle \mathbf{u}_h \rangle dV - \int_V \langle w'b' \rangle dV - \int_V \epsilon_{K^*} dV, \quad (13)$$

250 where the first term of the RHS of (13) comes from the development of (11). In a basin
 251 integrated sense, the time rate of change of IKE as diagnosed through ensemble statis-
 252 tics is thus a balance between exchanges with FKE, exchanges with eddy potential en-
 253 ergy, and dissipation ². It is not directly driven by prescribed forcing, but rather reflects
 254 the part of the ocean intrinsic dynamics that develops spontaneously in response to the
 255 non-linearity of the system. This provides an energy-budget based rationalization that
 256 the ensemble strategy provides an unambiguous definition of the ocean *turbulence*. In
 257 the following, we pay a particular attention to the contribution of EDDYFLX for the con-
 258 struction of IKE, and its relation to the mean flow (MEC) through the flux divergence
 259 DIVEF.

260 **2.2 Model and Simulations**

261 We analyze in this study a subset of the MEDWEST60 ensemble simulations (Leroux
 262 et al., 2021). These simulations have been produced to evaluate the predictability of the
 263 fine scale dynamics in a typical high-resolution Copernicus Marine Environment Mon-
 264 itoring Service (CMEMS) forecasting model by including the effect of initial and model
 265 uncertainties. It is based on a kilometric-scale regional configuration of the Western Mediter-
 266 ranean sea (cf Fig. 1) that uses the same numerical choices as the North Atlantic sim-
 267 ulation eNATL60 (Brodeau et al., 2020). Briefly, they are NEMO-v3.6 simulations run
 268 at $\frac{1}{60}^\circ$ and with vertical grid spacing of 1 m at the surface and 24 m at depth, for a to-
 269 tal of 212 vertical levels in MEDWEST60. The simulations are forced at the surface with
 270 3-hourly ERA-interim (ECMWF) atmospheric reanalysis through the CORE bulk flux
 271 formulation (Large & Yeager, 2004), and they partially account for ocean-atmosphere
 272 feedbacks (e.g., Renault, Molemaker, McWilliams, et al., 2016), where only 50% of sur-

² Note that in our setup, horizontal dissipation is implicitly included in the UBS advective scheme.

As detailed in Section 2.3, such a contribution is neglected when interpreting numerical results. For a theoretical understanding, however, it can be considered as part of the dissipative term of (13).

273 face currents speed is considered in the computation of the wind stress. Open bound-
 274 ary conditions are applied at the eastern and western boundaries of the domain with a
 275 Flow Relaxation Scheme (FRS) for baroclinic velocities and active tracers (Davies, 1976;
 276 Engedahl, 1995), and the "Flather" (Flather, 1994) radiation scheme for sea-surface height
 277 and barotropic velocities. The former is a simple relaxation of model fields toward hourly,
 278 externally-specified values over the 12 grid points adjacent to the boundaries. The re-
 279 laxation time scale ranges from $\tau = 0$ seconds at the domain edge and increases expo-
 280 nentially to about 30 days at grid point 12. The latter ("Flather") applies radiation con-
 281 ditions on the normal depth-mean transport across the open boundaries, set as prescribed
 282 values plus a correction based on sea surface height anomalies at the boundaries that al-
 283 lows gravity waves generated within the domain to exit through the open boundaries.
 284 We note that the prescribed boundary conditions are taken from the eNATL60 North
 285 Atlantic experiment run with tidal forcing, such that MEDWEST60 includes tides through
 286 boundary conditions in addition to tidal potential forcing.

287 Among the various ensemble simulations produced in the context of MEDWEST60,
 288 we focus here on the 20-member ensemble ENS-CI-GSL19, which has been produced as
 289 follows. From the already spun-up (through a 18 months integration) oceanic state of
 290 the eNALT60 simulation at February, 5th 2010, an ensemble of 20 runs has been pro-
 291 duced for 1 day with a stochastic perturbation (Brankart et al., 2015) applied on the hor-
 292 izontal grid of the model to represent uncertainties affecting the smallest scales in the
 293 model (for more details, see Leroux et al., 2021). The 20 oceanic states so generated have
 294 then been used as initial conditions for the production of a 120-day long, 20-member en-
 295 semble where all other components of the simulation (including forcing) are common across
 296 all members, and the stochastic perturbations are turned off. Such a procedure is usu-
 297 ally referred to as *micro* initial condition uncertainties (Stainforth et al., 2007; Hawkins
 298 et al., 2016), and is meant to allow the growth of dynamically consistent small pertur-
 299 bations.

300 **2.3 Diagnostic Considerations**

301 During the production of MEDWEST60 ensemble simulations, prognostic variables
 302 of the model (T, S, U, V, SSH), as well as vertical velocity (W), have been saved every
 303 hour. Based on these hourly averaged model outputs, we have used *offline* diagnostic
 304 tools to recompute the kinetic energy budget of MEDWEST60 simulations by closely fol-

305 lowing the numerical implementations of NEMO³. Relevant details for the present anal-
 306 ysis are provided in Appendix, along with validation. We note here that these *offline* tools,
 307 along with the high frequency of model outputs (hourly), provide us with a reliable pro-
 308 cedure to accurately (errors $\sim \mathcal{O}(10^{-3})$, see Table A1) compute the kinetic energy trends
 309 due to advection, thus the terms associated with eddy-mean kinetic energy transfers.

310 In our kinetic energy budget considerations derived in Section 2.1, we have assumed
 311 zero turbulent fluxes conditions at the boundaries of the domain. In practice, however,
 312 the computation of surface wind stress partially (50%) accounts for ocean-atmosphere
 313 feedback (Renault, Molemaker, McWilliams, et al., 2016), such that the turbulent wind
 314 work $\langle \mathbf{u}'_h \cdot \tau' \rangle$ is not strictly zero. This contribution is however weak (-0.12 TJ; 1 TJ =
 315 10^{12} J) as compared to mean wind work (+5.10 TJ) over the course of the 120-day long
 316 simulation, and is several orders of magnitude smaller than the total IKE production of
 317 +2.27 PJ (1 PJ = 10^{15} J) within the domain. Furthermore, this contribution is nega-
 318 tive, providing a sink for domain integrated IKE time rate of change, in agreement with
 319 the eddy-killing effect (Renault, Molemaker, Gula, et al., 2016). Similar considerations
 320 are also relevant for turbulent bottom stress, which damps the production of IKE. Our
 321 estimates of surface and bottom velocities ensemble spread suggest the bottom contri-
 322 bution is at least one order of magnitude weaker than the surface contribution. As for
 323 the open boundary conditions, the "Flather" scheme allows gravity waves generated within
 324 the domain to exit the model through boundaries, thus providing an explicit sink of IKE.
 325 In an averaged sense, all members are however expected to exhibit similar levels of en-
 326 ergy associated with the development of such waves, such that the spread so induced on
 327 model velocities is expected to be weak and can be neglected. We recall that baroclinic
 328 velocities are strongly relaxed toward prescribed values at the boundaries. The contri-
 329 bution of surface and boundary turbulent forcing, as well as bottom turbulent stress, for
 330 the interpretation of IKE production in our ensemble can then be safely neglected.

331 Finally, we are primarily interested in diagnosing eddy-mean flow kinetic energy
 332 transfers through the DIVEF, MEC and EDDYFLX terms of (11). As detailed above,
 333 open boundary conditions ensure that the ensemble spread at the boundaries is controlled,
 334 such that the domain integrated eddy fluxes of the cross energy term $\rho_0 \nabla \cdot \langle \mathbf{u}' (\langle \mathbf{u}_h \rangle \cdot \mathbf{u}'_h) \rangle$
 335 is negligible. This implies that all the energy released by the ensemble mean flow has been

³ These tools are part of the CDFTOOLS (<https://github.com/meom-group/CDFTOOLS.git>)

336 used to sustain the growth of IKE within the domain. We have tested this by comput-
 337 ing the volume integrated MEC and EDDYFLX terms for the full domain, and estimated
 338 their divergence DIVEF. We show on top panels of Figure 1 the vertically integrated MEC
 339 and EDDYFLX, and their divergence (DIVEF) is obtained by simple summation follow-
 340 ing (11). Integrated over the full domain, MEC drains -0.53 GW of energy out of the en-
 341 semble mean flow at that particular time (day 60), and EDDYFLX supplies +0.58 GW
 342 of energy to the turbulent flow. This confirms that our procedure provides reliable es-
 343 timates of these fluxes, with a $\sim 10\%$ error. This error, of about 0.05 GW, is relatively
 344 constant across the 20 ensemble members (± 0.01 GW, Figure 1, lower panel), suggest-
 345 ing this is a systematic error in our estimates. We attribute this error to the implicit dis-
 346 sipation of the UBS advective scheme used in MEDWEST60. As detailed in Appendix,
 347 we have performed the eddy-mean flow decomposition of the advective operator based
 348 on a 4th order centered scheme, which is the non-dissipative equivalent of the UBS scheme.
 349 The error in our estimates being positive and relatively constant across ensemble mem-
 350 bers, this suggests it is associated with dissipation.

351 In the following sections, we turn our attention to the analysis of the MEDWEST60-
 352 ENS-CI-GSL19 ensemble simulations, where we first diagnose the decorrelation of the
 353 turbulent flow from its ensemble mean, then evaluate the respective contribution of MEC
 354 and EDDYFLX for the kinetic energy budget of the ensemble mean and the turbulent
 355 flow, and then analyze their interactions through DIVEF.

356 **3 Results**

357 **3.1 Decorrelation of the Turbulent Flow**

358 Figure 2 provides horizontal maps and time evolution of surface kinetic energy, as
 359 well as its ensemble statistical decomposition. From left to right, the upper panels show
 360 the ensemble mean surface kinetic energy of the full flow $\langle K \rangle$, the FKE and the IKE at
 361 day 60. Their time evolution over the course of the 120 days, integrated within the green
 362 box, are shown on the lower panel. The ensemble mean full kinetic energy $\langle K \rangle$ exhibits
 363 a combination of high and low frequency variations, but remains relatively constant (6-
 364 8 TJ; 1 TJ= 10^{12} J) over the 120 days, reflecting the already spun-up state of the eNATL60
 365 simulation used to initialize the ensemble. For reference, the level of kinetic energy of
 366 a given member is shown in light gray. It exhibits small variations around its ensemble

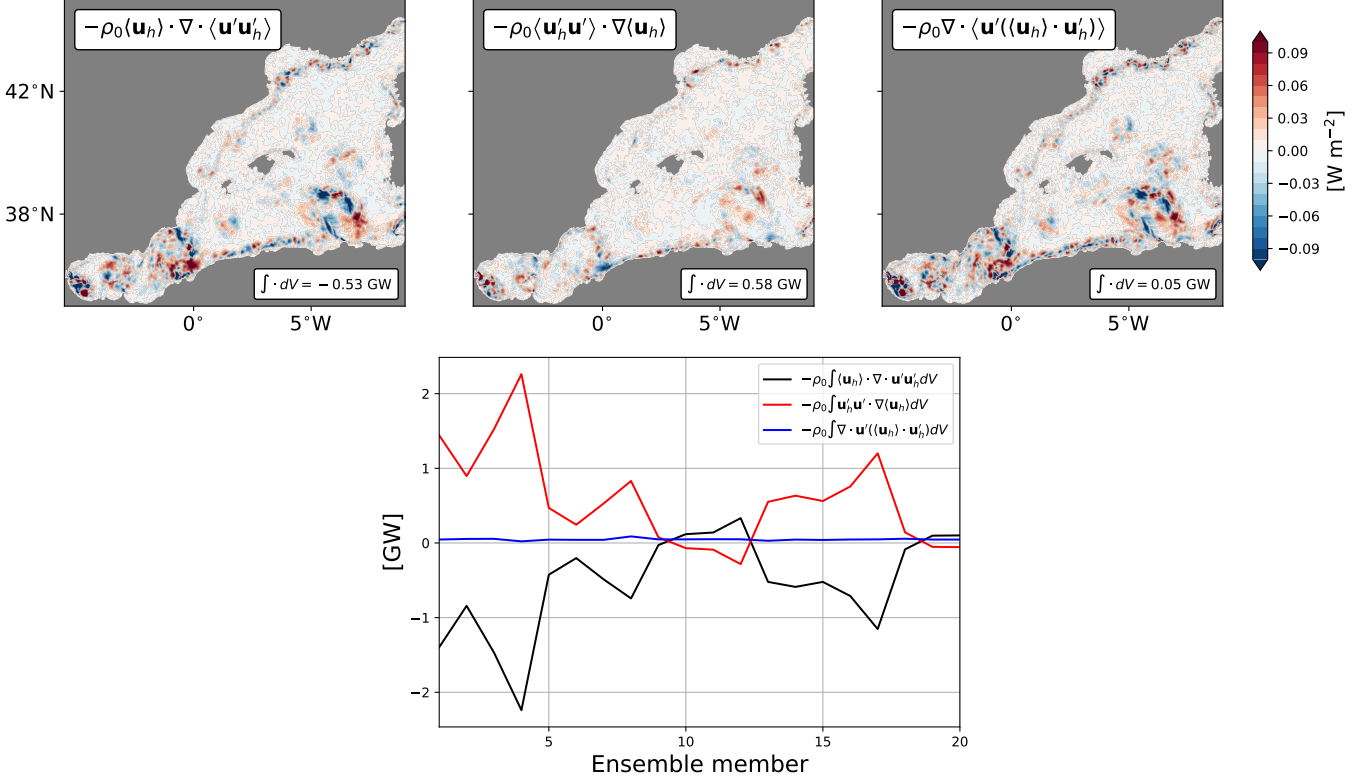


Figure 1. (Top panels) Vertically integrated MEC ($-\rho_0 \langle \mathbf{u}_h \rangle \cdot \nabla \cdot \langle \mathbf{u}' \mathbf{u}'_h \rangle$, left panel), EDDYFLX ($-\rho_0 \langle \mathbf{u}'_h \mathbf{u}' \rangle \cdot \nabla \langle \mathbf{u}_h \rangle$, center panel), and DIVEF ($-\rho_0 \nabla \cdot \langle \mathbf{u}' (\langle \mathbf{u}_h \rangle \cdot \mathbf{u}'_h) \rangle$, right panel) after 60 days of simulation. Their volume integrated values are shown at the bottom right of each panels. (Bottom panel) Basin integrated MEC (black), EDDYFLX (red) and DIVEF (blue) for each individual members.

367 mean equivalent, illustrating that the ensemble mean kinetic energy of the full flow pro-
 368 vides a statistical estimate of the energy level of the ensemble. We note that the devi-
 369 ation of the kinetic energy of a single member from the ensemble mean kinetic energy
 370 is not to be confused with the separation between the kinetic energy of the ensemble mean
 371 flow and that of the perturbations, which is the primary focus of our study.

372 The spatial pattern of the FKE (\tilde{K}) is representative of the relatively well orga-
 373 nized flow within the western Mediterranean basin. In the northern half, the FKE ex-
 374 hibits high levels of energy associated with the southwestward flowing Liguro-Provençal
 375 current (Millot, 1999; Waldman, 2016). In the southern half, FKE exhibits a very large
 376 import of energy through the strait of Gibraltar (exceeding 2000 J m^{-3}), the develop-
 377 ment of standing eddies downstream, and an eastward flowing boundary current along

378 the southern boundary of the basin (the Algerian Current, Millot, 1985). Around 5°E,
 379 this boundary current detaches from the coast, forming a 'loop current', a region of in-
 380 tense meso-scale eddies formation through mixed baroclinic-barotropic instabilities (e.g.
 381 Obaton et al., 2000; Poulain et al., 2021). We will focus on the eddy dynamics of this
 382 region in the following. Although more pronounced in the southern than in the north-
 383 ern part of the domain, the spatial organization of IKE ($\langle K^* \rangle$) somehow follows the spa-
 384 tial organization of FKE, reflecting the link between the two; turbulent dynamics develop
 385 in region of strong currents, which are more prone to instabilities.

386 The lower panel of Fig. 2 illustrates the time evolution of surface FKE and IKE,
 387 integrated within the green box, during the 120 days of simulation. At the beginning all
 388 ensemble members are in phase, such that IKE is zero and FKE reflects the energy con-
 389 tent of the full flow. The latter diverges from the ensemble mean full KE about one week
 390 after initialization as each ensemble member starts to decorrelate. At the end of the 120
 391 days, FKE has dropped to less than 2 TJ, i.e., about one third of its initial energy con-
 392 tent. In the same time, the turbulent part of the flow (IKE, $\langle K^* \rangle$) develops and reaches
 393 about 5 TJ at the end of the 120 days. This development exhibits several stages until
 394 it saturates after about 80 days. It is interesting to note that a first increase in IKE is
 395 observed from day 6 to day 20, where it reaches a first plateau. The 6 day time scale for
 396 the turbulent flow to start decorrelating from initial conditions is consistent with time
 397 scale reported by Fox-Kemper et al. (2008) and Schubert et al. (2020) in their idealized
 398 linear study of mixed layer instability and absorption of submesoscale vortices by mesoscale
 399 eddies, respectively. In both studies, time scales shorter than one week are associated
 400 with the development of submesoscale structures through surface mixed layer instabil-
 401 ities, which then saturate and undergo non-linear interactions to transfer their energy
 402 upscale. The 6 days time scale in our ensemble simulations is thus likely associated with
 403 similar processes, and suggests that the non-linear interactions of submesoscale insta-
 404 bilities are responsible for the initial growth of IKE. The other stages of IKE increase
 405 are associated with further development of turbulent flow. By comparing the IKE pat-
 406 terns at days 30 and 60 for instance (not shown), it appears that initial IKE develop-
 407 ment mostly takes place along the mean current, while later on, turbulent structures de-
 408 velop more broadly, contributing to the increase in the integrated IKE level within the
 409 green box. Further spectral estimates of the decorrelation of ensemble members over the
 410 first 60 days can be found in Fig. 6a of Leroux et al. (2021). In what follows, we will fo-

411 cus our analysis on day 60, which is about 20 days before the saturation of IKE. As shown
 412 in the following, this time period exhibits a well organized spatial structure in the eddy-
 413 mean flow KE interactions that nicely illustrates non-local processes. Such processes are
 414 nonetheless observed all along the 120-day long simulation ⁴.

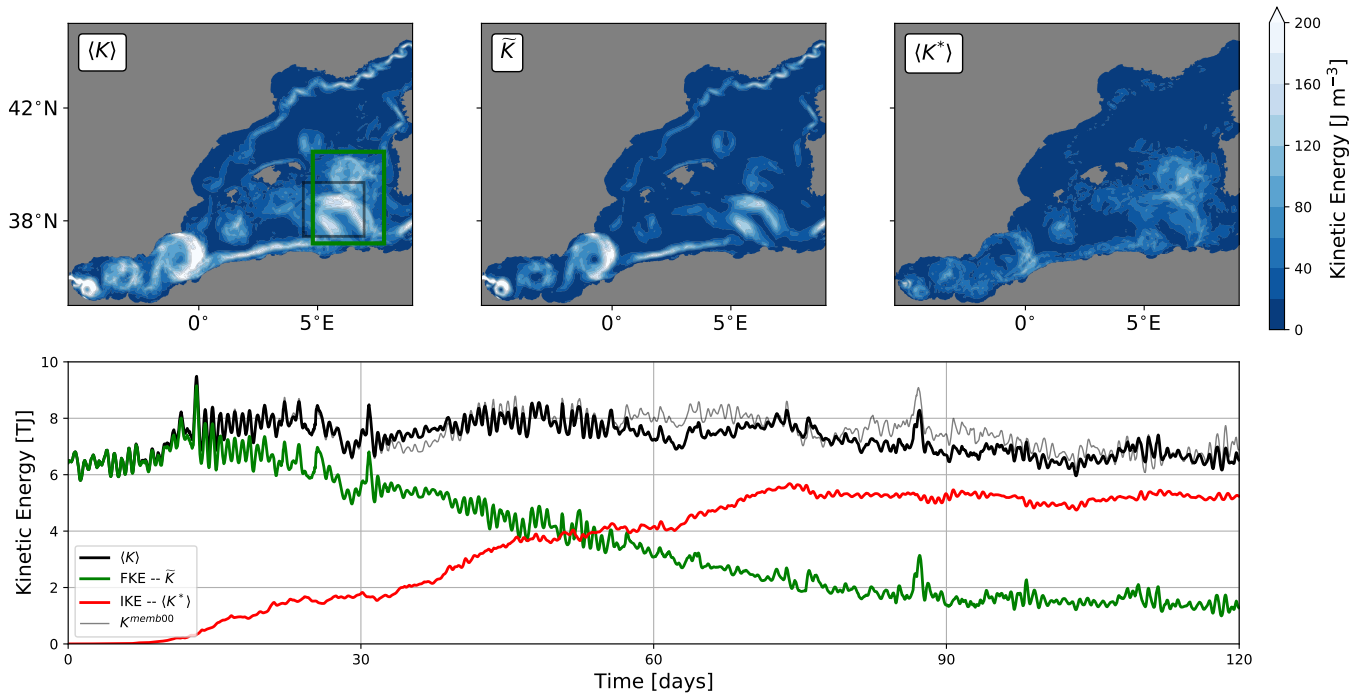


Figure 2. (Upper panels) Spatial maps of surface currents ensemble mean kinetic energy of the full flow ($\langle K \rangle$; left), kinetic energy of the ensemble mean flow (\tilde{K} , FKE; center) and the ensemble mean kinetic energy of the turbulent flow ($\langle K^* \rangle$, IKE; right) after 60 days of simulation. (Lower panel) 120-day long time series of these quantities, integrated within the green box. The time series of the kinetic energy of a given member is provided for reference (gray line). Units of the spatial maps are J m^{-3} and those of the time series are terrajoules ($1 \text{ TJ} = 10^{12} \text{ J}$). The black box on top left panel is used to validate our recomputation of kinetic energy budgets (cf Appendix).

⁴ The interested reader is referred to the following animation: [https://doi.org/10.5281/zenodo](https://doi.org/10.5281/zenodo.6221153)

415 3.2 Kinetic Energy Budget

416 We now turn our attention to the respective contributions of the advective terms
 417 of the FKE and IKE budget, focusing on the 'loop current' region. We recall here that
 418 many other processes contribute to these budgets, such as wave radiation, dissipation
 419 or exchanges with turbulent potential energy (cf (10)). We briefly discuss the contribu-
 420 tion of the latter in what follows, but otherwise postpone the analysis of other contri-
 421 butions for further work. Here, we focus our attention on the terms driving kinetic en-
 422 ergy transfers between the mean and the turbulent flow. We first discuss the kinetic en-
 423 ergy budget of the mean flow and that of the turbulent flow, and estimate the respec-
 424 tive contribution of MEC and EDDYFLX to these budgets.

425 We show on Fig. 3 the vertically integrated time rate of change of FKE (top left
 426 panel), as well as advection of FKE by the mean flow ($-\nabla \cdot \mathbf{u}\tilde{K}$; top right panel) and
 427 Mean-to-Eddy Conversion (MEC, $-\rho_0 \langle \mathbf{u}_h \rangle \cdot \nabla \cdot \langle \mathbf{u}'\mathbf{u}'_h \rangle$; bottom left panel) at day 60.
 428 Their vertical distributions within the upper 500 meters, horizontally integrated within
 429 the green box, appear on the bottom right panel as black, blue and red lines, respectively,
 430 and the contribution from other processes (computed as a residual) is shown in green
 431 ⁵. We first note that the time rate of change of FKE is dominated by a wave-like hor-
 432 izontal structure, which exhibits a strong baroclinic signature. The fast (daily) evolu-
 433 tion of this signal (not shown) suggests it is associated with the high frequency signal
 434 observed in the FKE time series of surface currents (Fig. 2, bottom panel). As part of
 435 the ensemble mean flow, this signal is likely associated with the forcing, such as high fre-
 436 quency winds and, to a smaller extend, tidal forcing. Integrated within the green box,
 437 this leads to a time rate of change of FKE of +0.30 GW. In contrast, both advection of
 438 FKE by the mean flow and MEC exhibit very different patterns with smaller scale struc-
 439 tures. The former exhibits a multipole-like organization, and its contribution tends to
 440 be of opposite sign in the upper 50 m (i.e., deeper than the ensemble mean and spatially
 441 averaged mixed layer depth of about 30 m) and the rest of the water column, such that
 442 when volume integrated, its contribution is two orders of magnitude weaker than the vol-
 443 ume integrated time rate of change of FKE. Although MEC exhibits weaker signal lo-

⁵ Note that all horizontal maps have been integrated down to the ocean floor for consistency, but most of the dynamics is observed within the upper 500 meters

444 cally, its volume integrated contribution is significant (-0.24 GW), with a maximum at
 445 about 40 m depth.

446 Fig. 4 shows the equivalent of Fig. 3 but for the IKE budget. We first note that
 447 the spatial pattern of IKE time rate of change is significantly different from that of FKE,
 448 with smaller scale structures. Contribution of advection of IKE by the mean and tur-
 449 bulent flow within the box is weak ($+0.03$ GW), but exhibits local important contribu-
 450 tions for the IKE redistribution. EDDYFLX contributes to $+0.25$ GW to the budget,
 451 which slightly exceeds the time rate of change of IKE of $+0.21$ GW. The vertical pro-
 452 file of turbulent potential to kinetic energy conversion rate $-\langle w'b' \rangle$ is also shown, with
 453 a net contribution within the green box of about $+0.20$ GW. It is maximum at about
 454 30 meters depth and tends toward zero at the surface. Although relatively weak when
 455 integrated within the green box (-0.08 GW), the large intensification of the residual near
 456 the surface is expected to mostly reflect the action of vertical viscous forces and dissi-
 457 pation.

458 Finally, we quantify the contribution of EDDYFLX for construction of the IKE over
 459 the course of the 120 days of simulations, and assess its relation with the loss of energy
 460 of the mean flow through MEC. This we address by computing the volume integrated
 461 contribution of both EDDYFLX and MEC within the green box of Fig. 2 for the 120 day
 462 long simulations. We show on Fig. 5 the time series of these two contributions (left panel),
 463 as well as their time integrated estimates (right panel). Starting from zero at the begin-
 464 ning of the simulations where all ensemble members are in phase, EDDYFLX starts to
 465 inject energy in the turbulent flow after about 5-6 days, in agreement with surface IKE
 466 increase discussed in Section 3.1. The rate at which EDDYFLX inject energy in the tur-
 467 bulent flow is of about 0.2 GJ s^{-1} with time variations as large as ± 0.13 GJ s^{-1} . MEC
 468 is draining energy out of the mean flow with similar rate and temporal variations, lead-
 469 ing to a small contribution of DIVEF (light blue line). Over the course of the 120 days
 470 of simulation, EDDYFLX and MEC have contributed to $+2.41$ PJ and -2.12 PJ for the
 471 IKE and FKE budget, respectively (Fig. 5, right panel). Within this region, the contri-
 472 bution of DIVEF is small, suggesting that eddy-mean energy transfers within this box
 473 are mostly local. Also shown on this figure is the contribution of the turbulent poten-
 474 tial to kinetic energy conversion rate $-\langle w'b' \rangle$. We first note the very large temporal vari-
 475 ations in this term as compared to eddy-mean flow interaction processes, suggesting in-
 476 tense exchanges with turbulent potential energy reservoirs on very short time scales. Their

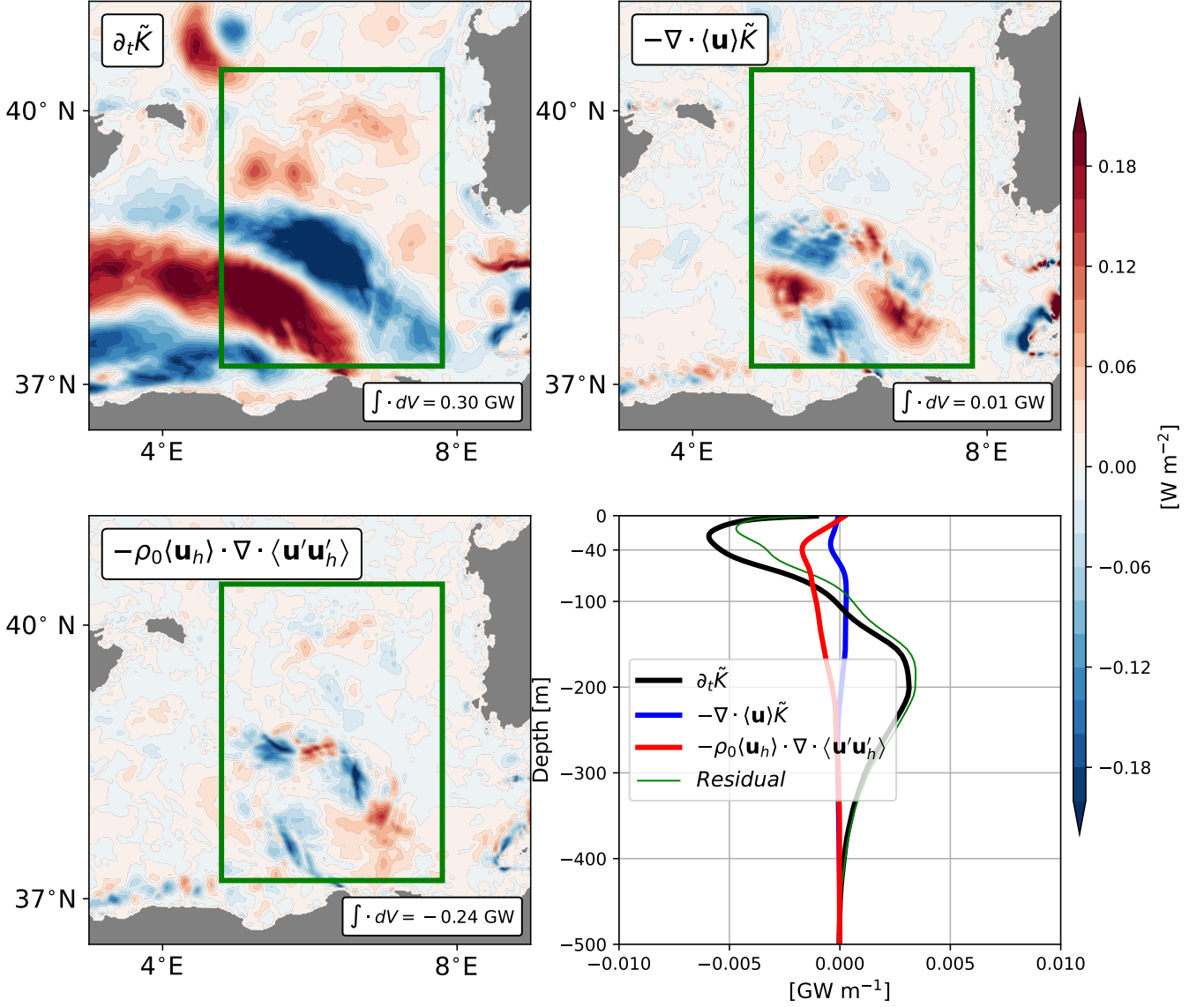


Figure 3. Vertically integrated time rate of change of FKE (upper left panel), advection of FKE by the mean flow (upper right panel) and Mean-to-Eddy energy Conversion rate (MEC, lower left panel) in the region of the loop current at day 60, with their volume integrated values within the green box shown at the bottom right of each panels. The vertical distribution of these quantities, within the upper 500 meters and horizontally integrated within the green box, are shown on the bottom right panel. The other components of the FKE budget are shown as a residual (green line).

477 time integrated contribution, however, is of the same order of magnitude than EDDYFLX
 478 but slightly weaker, supporting mixed barotropic-baroclinic instability processes for driv-

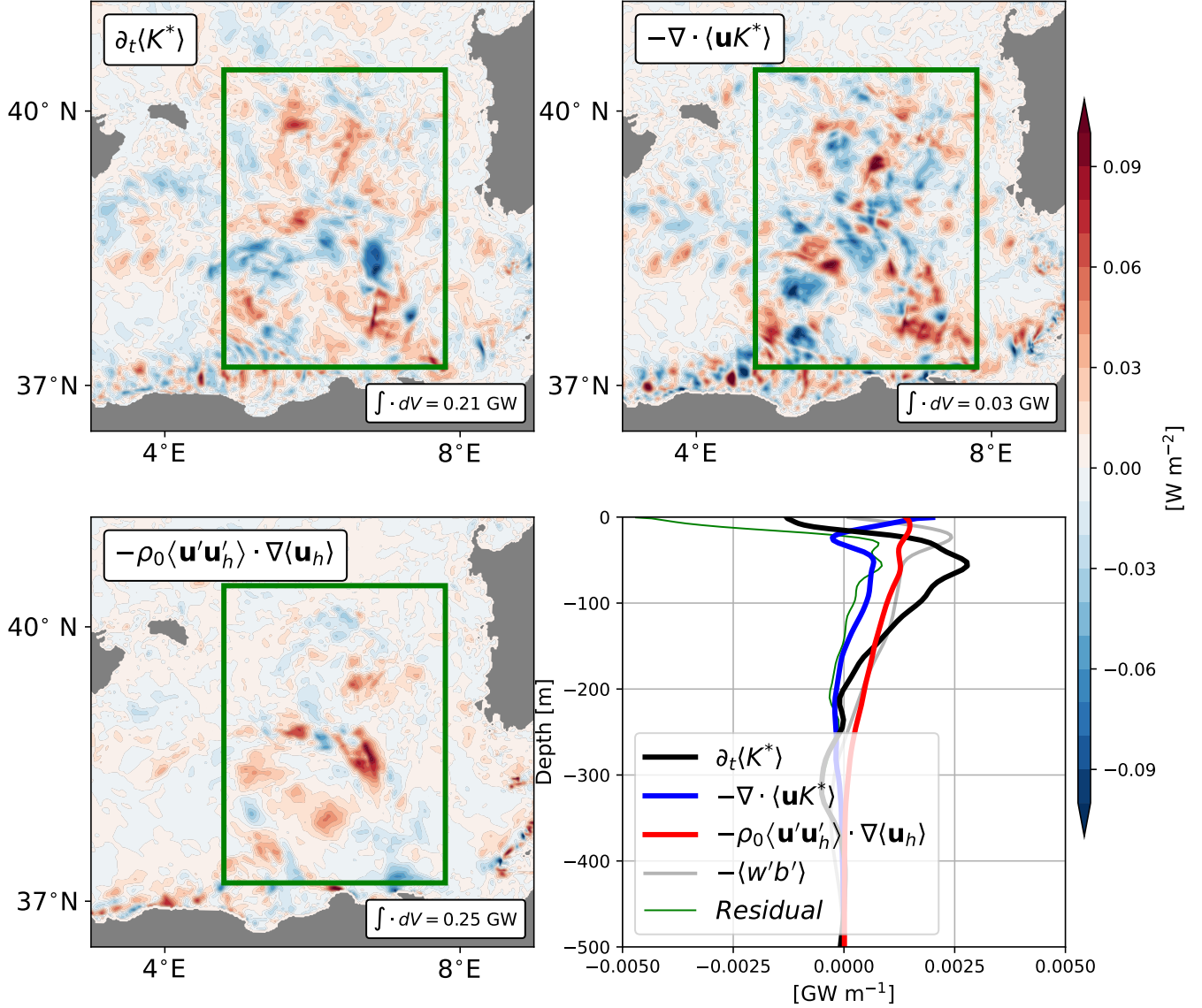


Figure 4. Same as Fig. 3, but for the IKE budget. The advection of IKE (upper right panel) includes advection by both the mean flow ($-\nabla \cdot \langle \mathbf{u} \rangle \langle K^* \rangle$) and the turbulent flow ($-\nabla \cdot \langle \mathbf{u}' K^* \rangle$). Turbulent potential to kinetic energy conversion rate ($-\langle w' b' \rangle$) is also shown in gray and its net contribution within the green box is of about +0.20 GW. Note the change in amplitude of the colorbar as compared to Fig. 3.

479 ing the growth of Algerian Eddies as proposed earlier (Obaton et al., 2000; Poulain et
 480 al., 2021). It is interesting to compare these estimates to the total IKE and FKE changes.
 481 During the 120 days of simulation, the volume integrated IKE within the green box has
 482 grown by +0.98 PJ, which is only about a quarter of the total energy injected by ED-

483 DYFLX and $-\langle w'b' \rangle$. Similarly, the FKE destruction over the full simulation is -0.91
 484 PJ, which is about half of the energy drained by MEC. This highlights the leading or-
 485 der contribution of other processes for balancing kinetic energy budgets of this region.

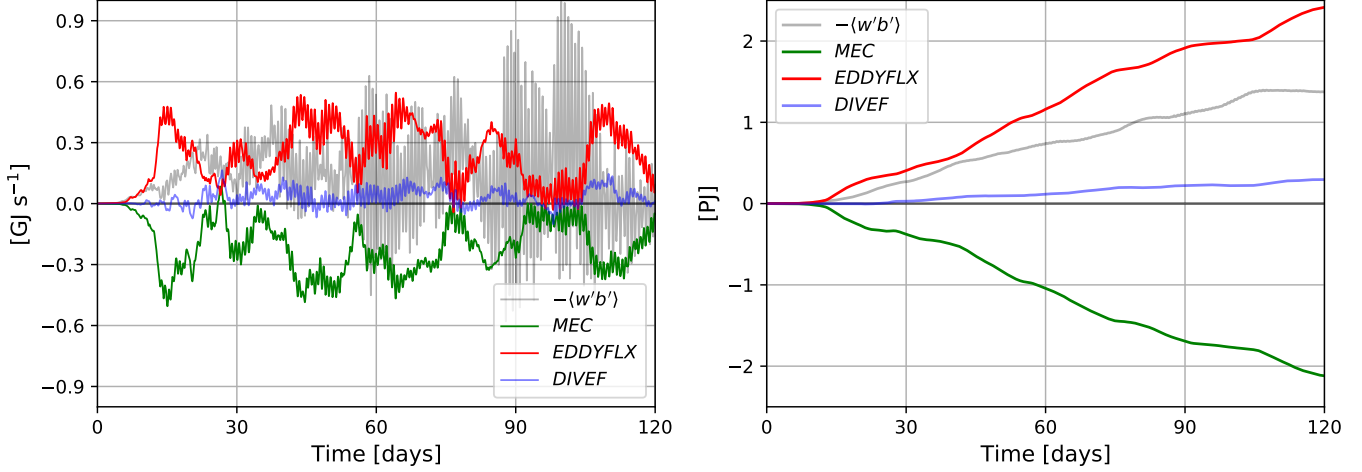


Figure 5. (Left) Time series of volume integrated MEC (green), EDDYFLX (red), DIVEF (light blue) and $-\langle w'b' \rangle$ (gray) within the green box of Fig. 2, and (right) their time integrated contribution. The 120-day long integrated MEC (EDDYFLX, DIVEF, $-\langle w'b' \rangle$) contribution is -2.12 PJ (+2.41 PJ, +0.30 PJ, +1.38 PJ).

486 4 Non-locality of FKE-IKE Energy Transfers

487 4.1 Diagnosing Non-Local KE Transfers

488 The patterns and amplitude of MEC and EDDYFLX discussed in the previous sec-
 489 tion are associated with energy transfers between the mean and the turbulent flow. As
 490 discussed in Section 2.1, this can reflect either local processes, with a negligible contri-
 491 bution of DIVEF (LHS of (11)), or non-local processes, with energy transfers with tur-
 492 bulent processes of remote regions if that term is not negligible. Dynamically, this pro-
 493 vides an estimate of the level of energy released by the mean flow that *locally* sustains
 494 the growth of eddies. Or, vice versa, an estimate of the level of energy released by the
 495 eddies that is *locally* backscattered to energize the mean flow. We further analyze this
 496 local vs non-local contribution in what follows.

497 Horizontal maps of vertically integrated MEC, EDDYFLX and DIVEF are shown
 498 in Figure 6 at day 60, and their volume integrated values within the green box appear

499 at the bottom right of each panel. Averaged over the box, the energy lost by the mean
500 flow (MEC, -0.24 GW) is used to support eddy growth (EDDYFLX, +0.25 GW), and
501 the divergence of eddy fluxes is weak (DIVEF, +0.01 GW). That MEC is draining -2.12
502 PJ out from FKE and EDDYFLX is injecting +2.41 PJ into IKE during the 120 days
503 of simulation, as diagnosed in Section 3.2, also supports that the turbulence that devel-
504 ops within the green box is largely controlled by local processes. However, the details
505 of these energy transfers is complex, and the radically different spatial structure of MEC
506 and EDDYFLX strongly suggests that eddy-mean flow kinetic energy transfers are non-
507 local at small scales. The spatial scale dependence of these non-local transfers is further
508 analyzed in Section 4.2.

509 At day 60, the horizontal structure of MEC (Fig. 6, left panel) exhibits alternation
510 of FKE destruction (blue spots) with FKE production (red spot), which tend to orga-
511 nize mostly along the mean flow. In contrast, EDDYFLX (Fig. 6, middle panel) exhibits
512 signals of weaker amplitude, which tend to be more pronounced on the flanks of the flow.
513 This suggests that a significant part of the kinetic energy lost by the mean flow at one
514 location is advected further downstream before being re-injected in the mean flow, but
515 little is used to sustain the growth of eddies locally. The connection between MEC and
516 EDDYFLX involves DIVEF, which is associated with eddy flux divergence of the cross
517 energy term $\langle \mathbf{u}_h \rangle \cdot \mathbf{u}'_h$. This term exhibits a rich spatial organization (Fig. 6, right panel),
518 with regions of destruction of FKE associated with a divergence of eddy fluxes, i.e., the
519 cross energy term is fluxed out of the control volume by the turbulent flow, and regions
520 of FKE production associated with a convergence of eddy fluxes, i.e., the cross energy
521 term is fluxed within the controlled volume by the turbulent flow. The region indicated
522 by the black line is of particular interest because it exhibits a region of production of IKE
523 (red spot of EDDYFLX) to the northeast of the region of FKE destruction. MEC, ED-
524 DYFLX and DIVEF vertical cross sections along this line are shown in Fig. 7. At the
525 surface, MEC exhibits its largest negative value about 10 km away from the core of the
526 mean current, and follows its tilted vertical structure. In contrast, the EDDYFLX is largest
527 about 20 km northeastward of the minimum of MEC, a region of strong horizontal mean
528 flow gradient, but exhibits a shallower vertical penetration as compared to MEC. As a
529 result, DIVEF is dominated by a divergence of eddy fluxes near the core of the mean flow,
530 and a convergence on its flank. Although a direct interpretation of a turbulent flux of
531 the cross energy term $\langle \mathbf{u}_h \rangle \cdot \mathbf{u}'_h$ to connect these regions of FKE destruction and IKE

532 production is tempting, we recall here that this term vanishes identically for turbulent
 533 flow orthogonal to the mean flow. This suggests that DIVEF is more efficient at trans-
 534 porting energy in the along stream direction than in the across stream direction, pro-
 535 viding a strong horizontal constraint for eddy-mean flow interactions. This may well pro-
 536 vide a dynamical rationalization to explain the large variations of MEC observed in the
 537 along stream direction, where energy extracted from the mean flow would be transported
 538 downstream before to be reinjected into the mean flow, but little would actually be trans-
 539 ferred to the turbulent flow through EDDYFLX.

540 Fig. 8 shows the horizontal and vertical contribution for the three components in-
 541 volved in eddy-mean flow kinetic energy transfers in the upper ocean layer. We first note
 542 that, as expected, vertical fluxes are much weaker than horizontal fluxes. However, while
 543 weak at each location, vertical turbulent fluxes are predominately positive in the upper
 544 layer, such that their horizontally integrated contribution is of the same order of mag-
 545 nitude than the horizontal turbulent fluxes for the three terms (Fig. 9). More interest-
 546 ingly, while the horizontal component of MEC and EDDYFLX tend to oppose each other,
 547 the vertical components tend to have the same sign. Indeed, the horizontal contribution
 548 of MEC is relatively constant and negative in the upper 100 meters and smoothly de-
 549 creases further below (left panel), while the horizontal contribution of EDDYFLX is neg-
 550 ligible at the surface, reaches its maximum at about 30 meters and smoothly decreases
 551 further below (center panel). In contrast, in both MEC and EDDYFLX, vertical turbu-
 552 lent fluxes are upward in the upper 15 meters, reach a maximum downward contribu-
 553 tion at the base of the spatially averaged mixed layer (about 30 meters), and decrease
 554 further below to reach negligible contribution below about 100 meter. The balanced DI-
 555 VEF within the green box (right panel) thus results in a balance between horizontal MEC
 556 and EDDYFLX below 100 meters, but involves strong contributions from the vertical
 557 turbulent fluxes within the upper 100 meters, with a prominent downward turbulent flux
 558 across the base of the of the mixed layer. Our results thus highlight the leading order
 559 contribution of vertical turbulent fluxes in eddy-mean flow kinetic energy interactions
 560 at the base of the mixed layer.

561 4.2 Horizontal Scale Dependence

562 Finally, we assess the scale-dependence of these non-local energy transfers. Although
 563 at small scales, our results suggest that eddy-mean flow interactions are largely non-local,

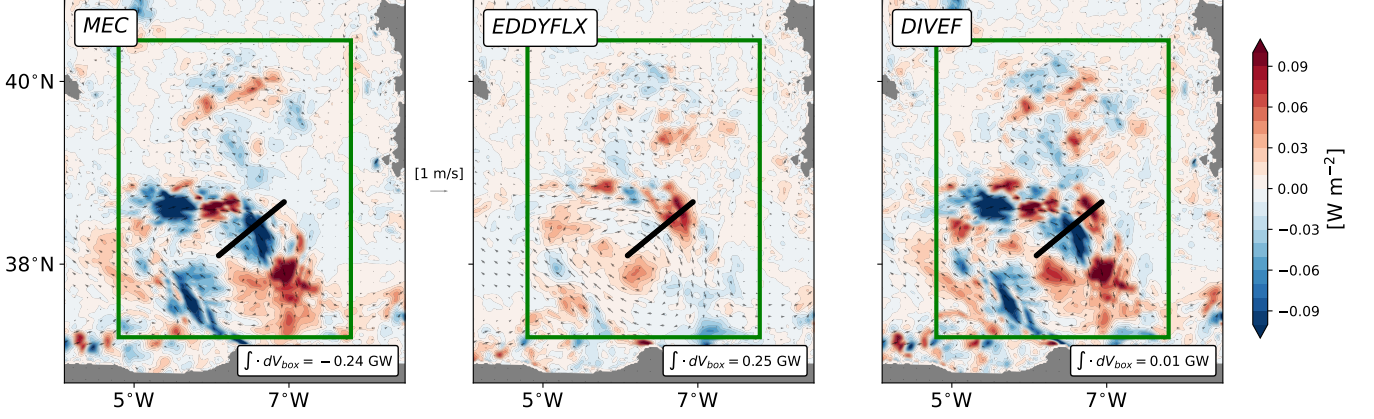


Figure 6. Vertically integrated MEC ($-\rho_0 \langle \mathbf{u}_h \rangle \cdot \nabla \cdot \langle \mathbf{u}' \mathbf{u}'_h \rangle$, left panel) EDDYFLX ($-\rho_0 \langle \mathbf{u}' \mathbf{u}'_h \rangle \cdot \nabla \langle \mathbf{u}_h \rangle$, middle panel) and DIVEF ($-\rho_0 \nabla \cdot \langle \mathbf{u}' (\langle \mathbf{u}_h \rangle \cdot \mathbf{u}'_h) \rangle$, right panel) after 60 days of simulations within the loop current region. Integrated quantities within the green box are shown on the bottom right insert. Ensemble mean surface currents are shown with arrows, and the black line is the section shown in Fig. 7.

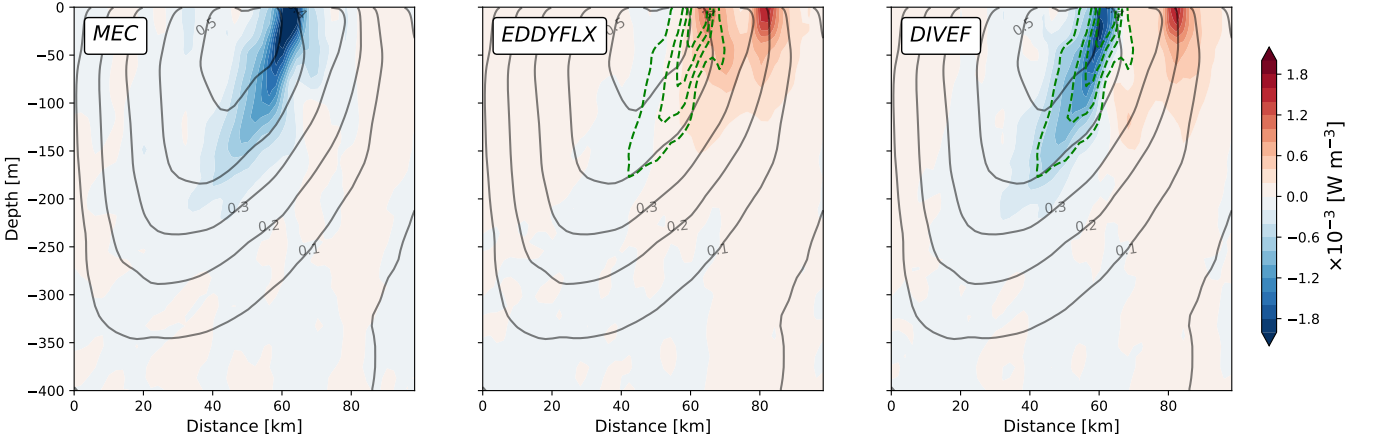


Figure 7. Associated vertical structure of MEC, EDDYFLX and DIVEF along the cross-stream section of Fig. 6. Gray contours represent the ensemble mean current across the section. Dashed green contours on middle and right panels show the main structure of MEC.

564 our estimates on larger scales tend toward a local balance (i.e., DIVEF is negligible). This
 565 is true for the $3^\circ \times 3^\circ$ green box of Fig. 6, as well as for other places in the western Mediter-
 566 ranean basin (not shown). This suggests non-local effects are predominantly small scale
 567 features, such that we are interested in quantifying their scale dependence. To test this,
 568 we have computed the spatial correlation r between MEC and EDDYFLX as a function

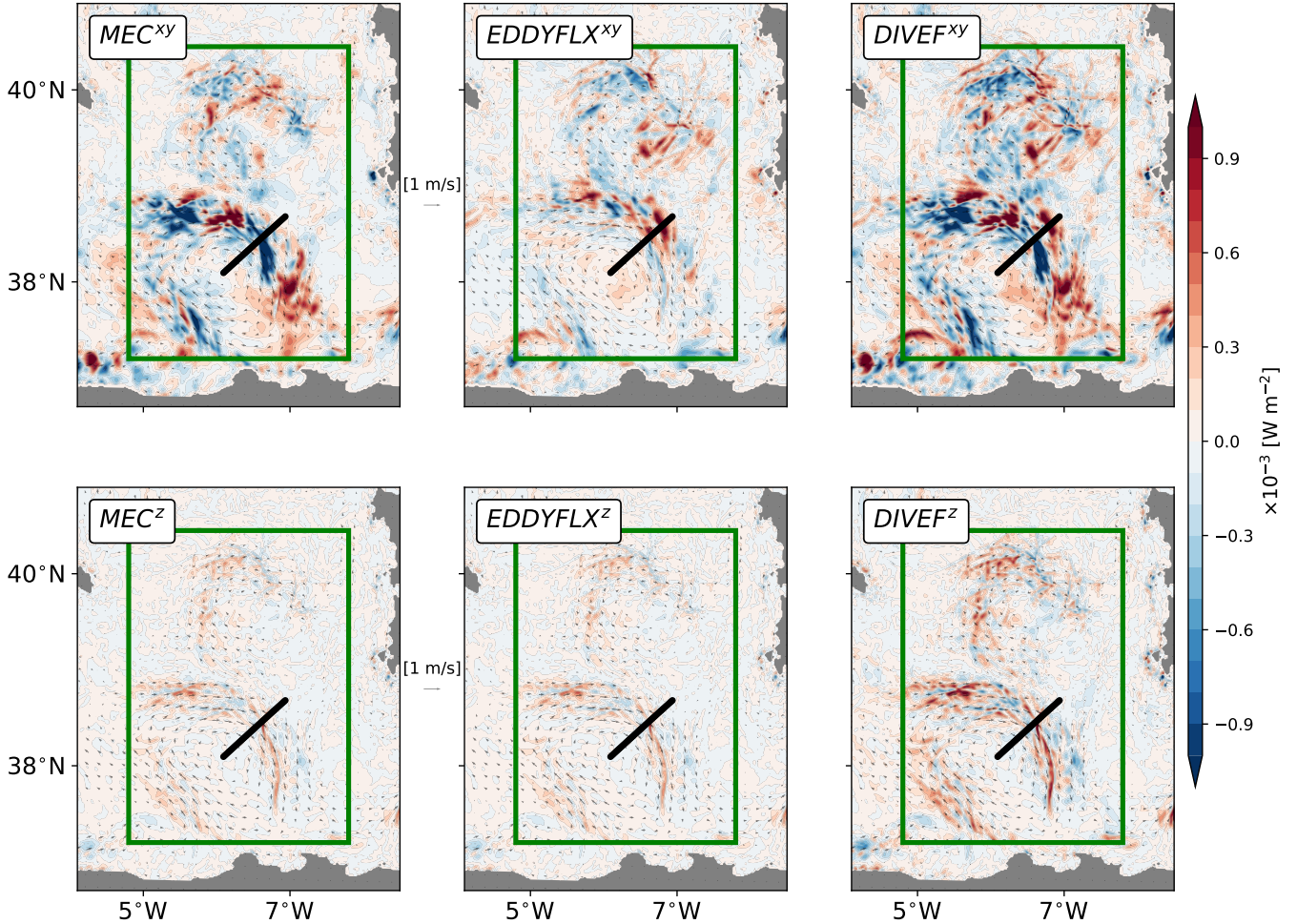


Figure 8. Upper layer MEC (left), EDDYFLX (center) and DIVEF (right) at day 60, decomposed into an horizontal (top panels) and a vertical (bottom panels) contribution. Ensemble mean surface currents are shown with arrows.

569 of coarse grained grid size (Figure 10). Starting from the initial model grid size at $\frac{1}{60}^\circ$,
 570 a spatial averaging is performed with the adjacent grid points, i.e., a factor 3, up to a
 571 grid size of about 4° . This procedure has been performed on four different boxes of $3^6 \times 3^6$
 572 (i.e., 729×729) grid points (colored lines) in order to cover the entire 883×803 grid points
 573 MEDWEST60 domain. The spatial correlation between MEC and EDDYFLX ranges
 574 from -0.12 on average at the model grid size to -0.96 at about 4° . This suggests that al-
 575 though non-local at small scales, kinetic energy transfers can be seen as local processes
 576 for scales larger than a few hundreds of kilometers. However, for eddy-resolving ocean
 577 models ($\sim \frac{1}{12}^\circ$), such as those that will equip the next generation climate models, non-

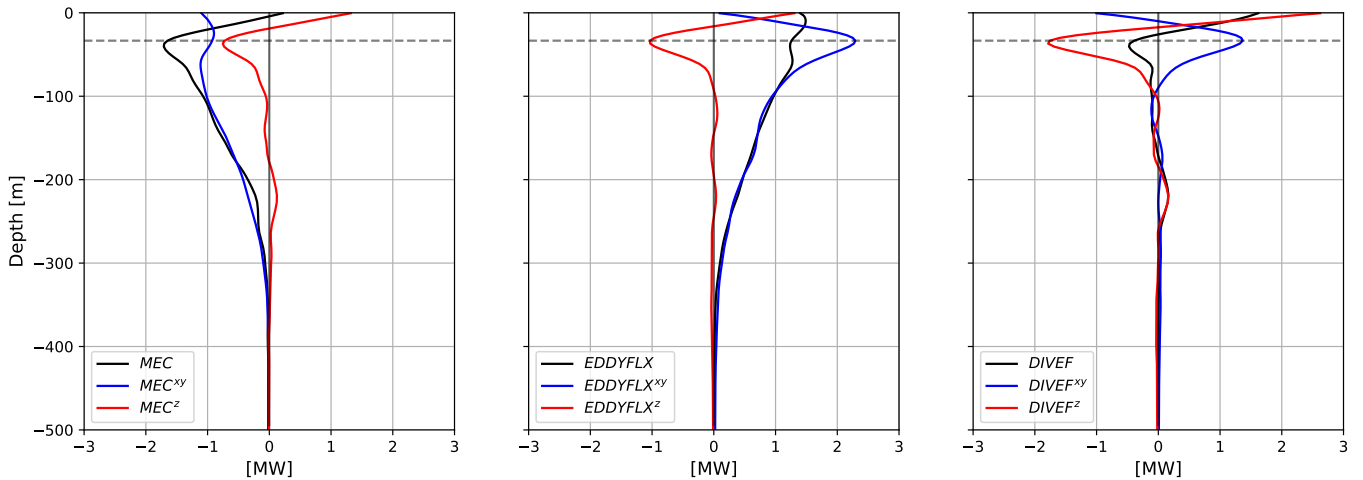


Figure 9. Vertical profile of horizontally integrated MEC (left), EDDYFLX (center) and DIVEF (right) within the green box of Fig. 6. Three-dimensional estimates (black) are decomposed into an horizontal (blue) and vertical (red) contribution. Positive vertical eddy fluxes are oriented upward, and the dashed gray line represent the spatially averaged mixed layer depth at about 30 meters.

578 local eddy-mean energy transfers are large ($r < -0.2$). This suggests that the processes
 579 associated with this non-locality need to be accounted for in the development of param-
 580 eterizations for eddy-resolving ocean models.

581 **5 Conclusion**

582 In this study, we have investigated the spatio-temporal structure of the kinetic en-
 583 ergy transfers between the ensemble mean and the turbulent flow. We have performed
 584 our analysis with a kilometric-scale resolution ($\frac{1}{60}^\circ$), 120-day long, 20-member ensem-
 585 ble simulations of the Western Mediterranean basin (Leroux et al., 2021). We have first
 586 introduced the Forced and Internal Kinetic Energy equation (FKE and IKE, respectively)
 587 in this framework, and discussed the implications for their interpretation. In particular,
 588 the prescribed surface and boundary forcings drive the basin integrated time rate of change
 589 of FKE, and the basin integrated time rate of change of IKE reflects the energy of the
 590 turbulent flow that develops within the domain through the non-linear dynamics sen-
 591 sitive to initial conditions. We have then quantified the respective contributions of Mean-
 592 to-Eddy energy Conversion (MEC, $\langle \mathbf{u}_h \rangle \cdot \nabla \cdot \langle \mathbf{u}'_h \mathbf{u}'_h \rangle$) and the EDDY momentum FLuX
 593 (EDDYFLX, $\langle \mathbf{u}'_h \mathbf{u}'_h \rangle \cdot \nabla \langle \mathbf{u}_h \rangle$) in the FKE and IKE budgets during the 120-day long runs.

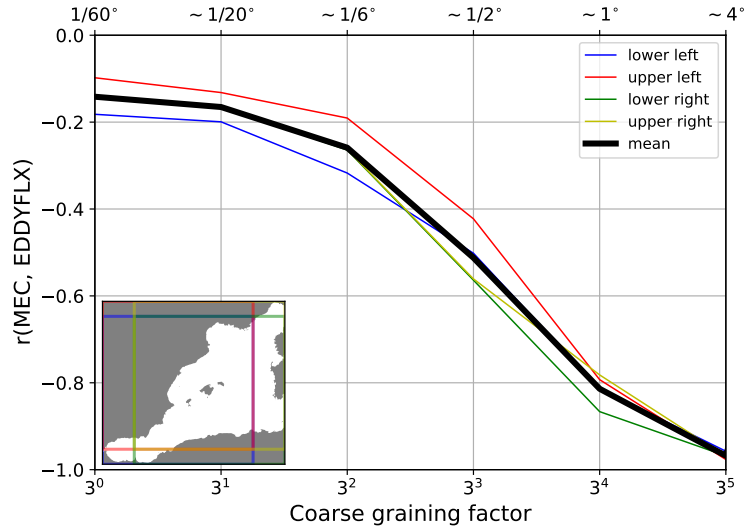


Figure 10. Spatial correlation of MEC and EDDYFLX as a function of the coarse grained grid size at day 60. The local vs non-local computation is made on four $3^6 \times 3^6$ regions (color lines and insert) and the results averaged (black line). The associated coarse grained grid size is shown on top axis.

594 By further analyzing their spatial organization, we have then highlighted the non-locality
 595 of the energy transfers between the ensemble mean and the turbulent flow, where non-
 596 local processes are associated with energy destruction in one reservoir that does not *lo-*
 597 *cally* sustain the growth of kinetic energy in the other reservoir, in agreement with pre-
 598 vious studies (Chen et al., 2014; Kang & Curchitser, 2015; Capó et al., 2019). We have
 599 pointed out to the leading contribution of the DIVERgence of Eddy Fluxes (DIVEF, $\nabla \cdot$
 600 $\langle \mathbf{u}'(\langle \mathbf{u}_h \rangle \cdot \mathbf{u}'_h) \rangle$) as a key component in this non-local transfers. Our main contribution
 601 is to recognize that this term is associated with advection of the cross energy term $\langle \mathbf{u}_h \rangle \cdot$
 602 \mathbf{u}'_h by the turbulent flow, which provides a strong spatial constraint on these transfers
 603 since the cross energy term vanishes identically for turbulent flow orthogonal to the mean
 604 flow. Finally, we have shown that although weaker than the horizontal component at the
 605 model grid size, the vertical eddy fluxes become leading order when horizontally inte-
 606 grated over sufficiently large scales. On average, their contribution is to flux energy (mean,
 607 eddy and cross energy term) downward across the base of the mixed layer.

608 Analyzing the scale dependence of these non-local KE transfers, we have shown that,
 609 although prevalent at eddy scales, they tend toward a local balance at non-eddy scale

610 (i.e., $> 1^\circ$). Thus, while our results support approximations usually made in the devel-
 611 opment of energy-aware parameterizations of meso-scale turbulence (Eden & Greatbatch,
 612 2008; Mak et al., 2018; Jansen et al., 2019), i.e., that the growth of sub-grid scale tur-
 613 bulent kinetic energy is locally sustained by a destruction of kinetic energy of the resolved
 614 flow, they point out to the necessity of accounting for this non-local dynamics for the
 615 development of parameterizations for eddy-resolving ocean models, such as those that
 616 will equip next generation climate models. In this direction, the emerging approach of
 617 *transport under location uncertainty* for the representation of small scale, stochastic dy-
 618 namics and its effect on the large scale flow (e.g., Mémin, 2014; Resseguier et al., 2017;
 619 Chapron et al., 2018) is an attractive alternative to the mixing length approach.

620 Finally, we want to discuss the implications of our results for the interpretation of
 621 the dynamics of western boundary currents jet extension such as the Gulf Stream. Jamet
 622 et al. (2021) have recently shown the leading order contribution of MEC for the ener-
 623 getic balance of the North Atlantic subtropical, wind driven gyre. They concluded that
 624 MEC in the Gulf Stream extension region is the primary sink of 26-year mean kinetic
 625 energy within the gyre, balancing the energy inputted by the wind in the westerly wind
 626 region of the North Atlantic subtropical gyre. However, how this loss of mean kinetic
 627 energy interacts with the turbulent flow remains an open question. Some indications of
 628 spatial organization of EDDYFLX can be found in previous in-situ and satellite obser-
 629 vation analyzes. In their earlier work on Gulf Stream energetics based on in-situ obser-
 630 vations, Webster (1961, 1965), Rossby (1987) and Dewar and Bane (1989) have reported
 631 on eddy fluxes that are more pronounced on the inshore flank of the Gulf Stream, both
 632 along the US coastline and downstream of Cap Hatteras. Based on satellite observations,
 633 Ducet and Le Traon (2001) and Greatbatch et al. (2010) have highlighted a prominent
 634 feature of the Gulf Stream, so-called the 'double-blade' structure, associated with the
 635 turbulent dynamics just downstream of Cape Hatteras. There, the Reynolds stress cross-
 636 covariance was found to be maximum on both flanks on the stream, and to exhibit al-
 637 ternation of highs and lows further downstream. This 'double-blade' structure suggests
 638 that eddy fluxes (EDDYFLX) are more pronounced on the flank of the jet, where large
 639 Reynolds stresses $\overline{u'v'}$ are colocalized with a strong horizontal shear of the mean flow
 640 $\partial_y \bar{u}$, while mean-to-eddy conversion rates (MEC) would be more pronounced toward the
 641 core of the jet, where the cross-stream gradient of Reynolds stresses $\partial_y \overline{u'v'}$ are colocal-
 642 ized with maximum of the mean zonal current \bar{u} . We can also find some indications of

643 such a spatial organization of eddy-mean flow interactions in the Lorenz energy cycle based
644 on eddy-resolving numerical simulations of Kang and Curchitser (2015), although fur-
645 ther analyses are needed to conclude on this.

646 **Appendix A Offline Recomputation of Kinetic Energy Budget**

647 We are interested in analyzing the energetic of the MEDWEST60 ensemble sim-
648 ulations, which have been recently produced (Leroux et al., 2021). We thus developed
649 diagnostic tools to recompute the momentum budget, which kinetic energy builds upon,
650 of these simulations based on the variables saved during the production of these simu-
651 lations, i.e. three-dimensional temperature (T), salinity (S) and velocity (U, V, W), as
652 well as two-dimensional free-surface elevation (SSH). These *offline* tools are developed
653 as part of the CDFTOOLS diagnostic package for the analysis of NEMO model output
654 (<https://github.com/meom-group/CDFTOOLS.git>), which are written in FORTRAN
655 90 and follow the numerical implementation of the NEMO General Circulation Model
656 (Madec et al., 2017).

657 As all GCM, NEMO offers different numerical schemes to integrate the Primitive
658 Equations with various levels of approximation. The numerical schemes that have cur-
659 rently been implemented in these tools are those relevant for the analysis of the ener-
660 getic of the MEDWEST60 ensemble simulations, which are based on the version 3.6 of
661 the NEMO model. This includes: A dynamical vertical coordinate following the free sur-
662 face elevation, with partial stepping along the ocean floor; the third order upstream bi-
663 ased scheme (UBS, Shchepetkin & McWilliams, 2005) to advect momentum; the TEOS-
664 10 equation of state (Roquet et al., 2015) to compute density; a split-explicit formula-
665 tion to compute surface pressure gradients (Shchepetkin & McWilliams, 2005), which
666 also accounts for atmospheric surface pressure loading and freshwater air-land-sea fluxes;
667 and an implicit time differencing scheme to compute vertical viscous effects, which in-
668 clude surface wind stress forcing following the CORE bulk flux formulation (Large & Yea-
669 ger, 2004), bottom friction due to bottom boundary condition, tides, internal waves break-
670 ing and other short time scale currents, as well as vertical dissipation of momentum within
671 the water column based on the Turbulent Kinetic Energy (TKE) turbulent closure scheme
672 (Mellor & Yamada, 1982; Gaspar et al., 1990; Blanke & Delecluse, 1993). A full descrip-
673 tion of these schemes is available online ([https://github.com/quentinjamet/CDFTOOLS/
674 blob/cdfdyn/note_KE_bgt_cdftools.pdf](https://github.com/quentinjamet/CDFTOOLS/blob/cdfdyn/note_KE_bgt_cdftools.pdf)). With shorthands, the full kinetic energy bud-

675 get can be represented as:

$$NXT = ADV + (HPG + SPG_{1st\ guess}) + SPG_{correction} + ZDF, \quad (A1)$$

676 where NXT refers to the time rate of change ∂_t (before application of the Asselin fil-
 677 ter), ADV to three-dimensional advection, HPG to hydrostatic pressure work, $SPG_{1st\ guess}$
 678 to surface pressure work computed at baroclinic time step due to the rescaled vertical
 679 coordinate following free surface elevation, $SPG_{correction}$ to surface pressure work cor-
 680 rection associated with the time-splitting scheme of Shchepetkin and McWilliams (2005)
 681 which includes atmospheric pressure loading and freshwater fluxes, and ZDF to verti-
 682 cal viscous effects.

683 **A1 Validation at Model Time Step**

684 In order to insure that our offline recomputation lines up with the online estimates
 685 computed by the NEMO model, we have re-run for a short period of time one member
 686 of the ensemble and outputted, at the model time step ($\Delta t = 80s$), momentum and ki-
 687 netic energy trends, as well as required prognostic variables necessary for their offline re-
 688 computation, within the 150x150 grid point sub-region (black box on Fig. 2). Compar-
 689 ing our offline recomputation with the online estimates provides an robust estimate of
 690 the errors. An example is provided on Fig. A1 for the three-dimensional advection of ki-
 691 netic energy within the model upper layer. The errors are relatively small (locally four
 692 order of magnitude, but five order of magnitude when horizontally averaged within the
 693 sub-domain, cf Table A1), providing strong confidence in the accuracy of these tools. Tests
 694 for the other terms of the KE budget have been conducted, providing similar level of ac-
 695 curacy for time rate of change and pressure work (cf Table A1). Offline estimates of ver-
 696 tical viscous effects are associated with much larger errors, of the order of 10%, and we
 697 currently have no estimates for the surface pressure correction associated with the split-
 698 explicit scheme.

699 **A2 Estimation of Errors Due to Time Discretization and Averaging**

700 Based on model time step accuracy estimates, we have quantified the errors asso-
 701 ciated with time discretization of the different operators, as well as the use of time av-
 702 eraged quantities. We discuss here these implications for the estimates of the advective
 703 component of the budget.

704 The advective operator used in the MEDWEST60 is an upstream biased third or-
705 der scheme (UBS, Shchepetkin & McWilliams, 2005). This scheme has two component,
706 a second order scheme and a third order biased scheme. While the former is centered
707 in time, the latter is implemented forward in time, i.e. it is evaluated with *before* veloc-
708 ities. While this numerical detail provides stability for a GCM, it is not required in the
709 context of *offline* computations and introduces ambiguities about how this should be eval-
710 uated when working with time averaged quantities. We thus decided to evaluate the third
711 order biased scheme of the advective operator as centered in time instead. This leads to
712 a growth of the errors made in the recomputation by one order of magnitude (cf Table A1).
713 When computed based on hourly model outputs, as available from MEDWEST60, the
714 error increases by another order of magnitude to reach 10^{-3} . Also increased from model
715 time step to hourly model outputs, the accuracy of these *offline* diagnostic tools remains
716 high, providing reliable estimates of the advective operator of the model. Similar con-
717 siderations are applied for the vertical viscous effects (i.e. time discretization, hourly model
718 outputs), but the already large error of 10^{-1} is found to be unchanged.

719 Finally, we estimate the evolution in time of these errors by comparing the recom-
720 putation made with hourly model outputs with estimates outputted by the model over
721 a time period of 10 days (Figure A2). From these tests, no systematic errors emerged
722 for both time rate of change (upper left panel) and hydrostatic pressure work (bottom
723 left panel). We observe, however, a steady growth in the error made in the recomputa-
724 tion of the advective term (top right panel), reaching about -20×10^{-3} GW h $^{-1}$ at the
725 end of the 10 days of simulation. Finally, the largest errors are observed in the recom-
726 putation of the vertical viscous effects (bottom right panel), in agreement with errors
727 reported earlier. We are currently working on improving this recomputation.

728 A3 Eddy-mean Separation

729 Based on these *offline* estimates, we explicitly decompose the full equation into mean
730 and eddy contributions. For the zonal momentum advection, it leads to:

$$\nabla \cdot \mathbf{u}u = \nabla \cdot \langle \mathbf{u} \rangle \langle u \rangle + \nabla \cdot \langle \mathbf{u} \rangle u' + \nabla \cdot \mathbf{u}' \langle u \rangle + \nabla \cdot \mathbf{u}' u' \quad (\text{A2})$$

731 where $\langle \cdot \rangle$ and $'$ denotes averaging and perturbation, respectively (cf Section 2.1 for de-
732 tails on the decomposition used in this study). Performing a similar procedure for the
733 advection of meridional momentum, multiplying the former by $\rho(\langle u \rangle + u')$ and the lat-

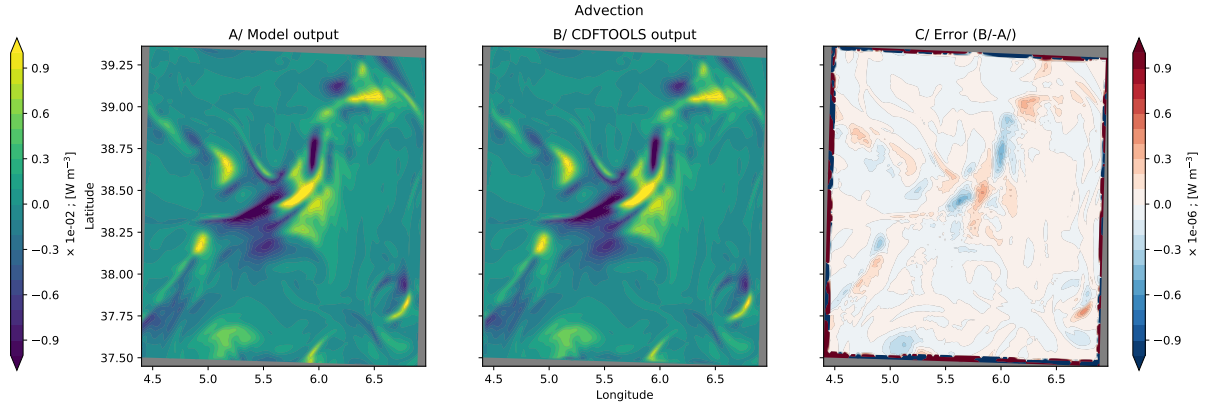


Figure A1. Upper layer Kinetic Energy trends associated with three-dimensional advection based on the model outputs (left), its offline recomputation (center), and associated errors (right). The *offline* recomputation is performed at model time step and accounts for the forward time discretization of the third order upstream biased part of UBS advective scheme. Note the different scale factor used for errors.

734 ter by $\rho(\langle v \rangle + v')$ and summing the resulting equations leads to a decomposition of the
 735 advection of kinetic energy that accounts for the different contributions that compose
 736 the FKE and IKE budgets (equations (8) and (9), respectively). We note here that in
 737 MEDWEST60, the advection of momentum is achieved by the upstream biased third or-
 738 der scheme (UBS, Shchepetkin & McWilliams, 2005). This scheme accounts for the hor-
 739 izontal dissipation of momentum through an implicit formulation which takes the form
 740 of a biharmonic operator with an eddy coefficient proportional to the velocity $A_h = -|u|\Delta x^3/12$.
 741 The formulation of this implicit dissipation introduces complexities in the eddy-mean
 742 decomposition. We thus decided to evaluate the horizontal advection terms using a 4th
 743 order finite differencing centered scheme instead, which is the non-dissipative equivalent
 744 of the UBS scheme (Jouanno et al., 2016; Madec et al., 2017).

745 Acknowledgments

746 This work was supported through the French ‘Make Our Planet Great Again’ program
 747 managed by the Agence Nationale de la Recherche under the Programme d’Investissement
 748 d’Avenir, with the reference ANR-18-MPGA-0002. MEDWEST60 ensemble simulations
 749 and their analyses have been performed using HPC resources from GENCI-IDRIS through

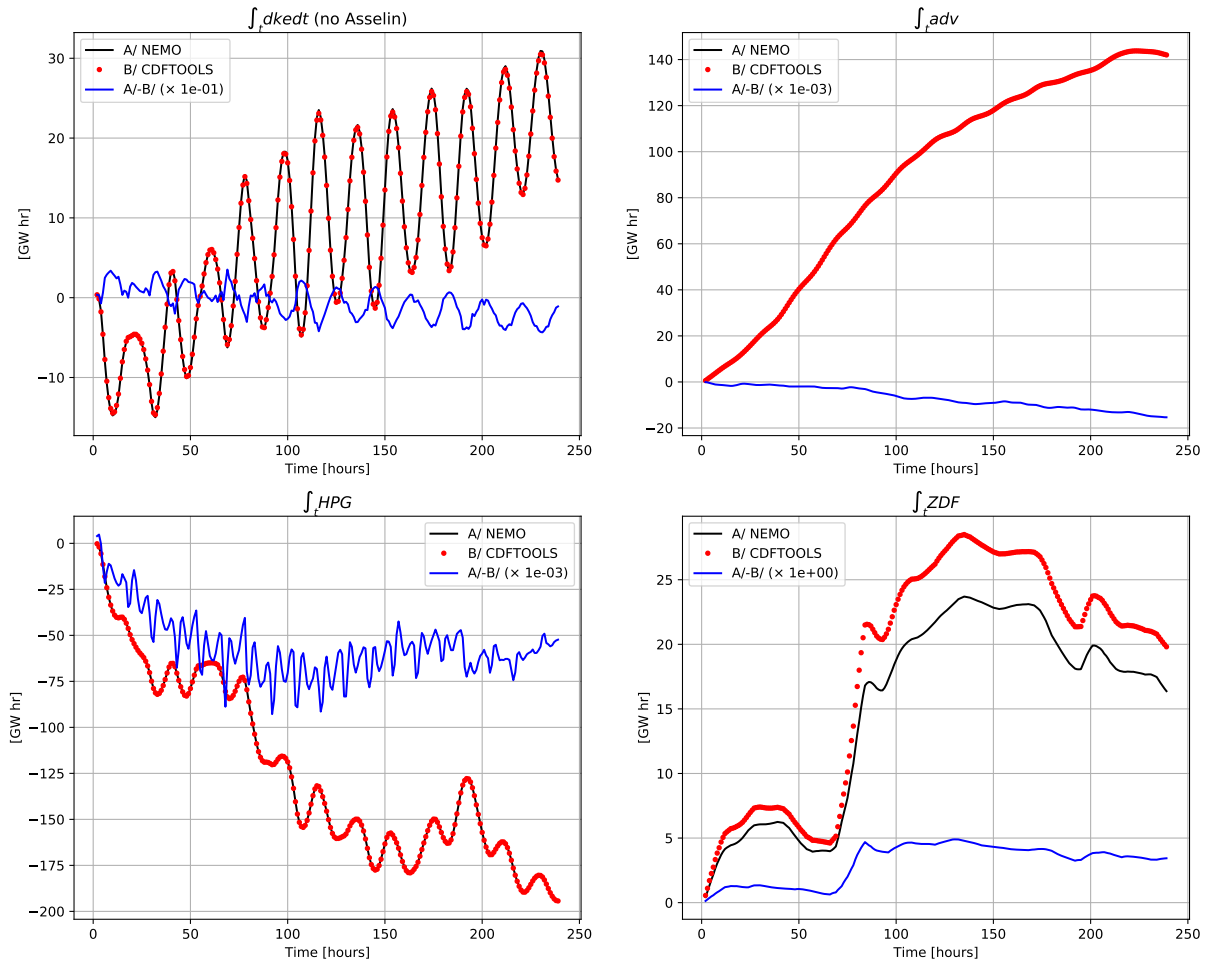


Figure A2. Time integrated KE trends of the full sub-domain, volume integrated time rate of change (upper left), three-dimensional advection (upper right), pressure work (bottom left) and vertical dissipation (bottom right) based on hourly averaged model outputs (black lines), recomputation based on hourly averaged T, S, U, V, W, η (red dots), and the associated errors (blue lines). Note the scale factor used for errors in the legend panels, which differs for each quantities.

Table A1. Order of magnitude of the errors of the offline estimates for the different terms of the kinetic energy budget, computed as the spatial root-mean-square error normalized by the spatial standard deviation of the reference, NEMO outputs. The third line stands for the sensitivity of the error associated with the forward time discretization of the third order upstream biased part of UBS advective scheme and in the TKE turbulent closure scheme. We currently have estimates for the surface pressure work correction associated with the split-explicit scheme (third term of the RHS), such that no values are reported on here.

	$\partial_t K$	$= - \nabla \cdot \mathbf{u}K$	$- \mathbf{u}_h \cdot \nabla_h \phi_{hyd}$	$- \mathbf{u}_h \cdot \nabla_h \phi_{surf}$	$+ \rho_0 \mathbf{u}_h \cdot \mathbf{D}^m$
Model time step	10^{-3}	10^{-5}	10^{-5}	–	10^{-1}
Time discretization	–	10^{-4}	–	–	10^{-1}
Hourly average	10^{-2}	10^{-3}	10^{-3}	–	10^{-1}

750 the Grant A008-0111279 allocated in the context of the H2020-IMMERSE projet (Eu-
 751 ropean Union Horizon 2020 research and innovation programme, grant No 821926).

752 **References**

753 Aluie, H., Hecht, M., & Vallis, G. K. (2018). Mapping the energy cascade in the
 754 North Atlantic Ocean: The coarse-graining approach. *J. Phys. Oceanogr.*,
 755 *48*(2), 225–244.

756 Blanke, B., & Delecluse, P. (1993). Variability of the tropical Atlantic Ocean simu-
 757 lated by a general circulation model with two different mixed-layer physics. *J.*
 758 *Phys. Oceanogr.*, *23*(7), 1363–1388.

759 Brankart, J.-M., Candille, G., Garnier, F., Calone, C., Melet, A., Bouttier, P.-A.,
 760 Brasseur, P., and Verron, J. (2015). A generic approach to explicit simulation
 761 of uncertainty in the nemo ocean model. *Geoscientific Model Development*,
 762 *8*(5), 1285–1297.

763 Brodeau, L., Le Sommer, J., & Albert, A. (2020). Ocean-next/eNATL60: Mate-
 764 rial describing the set-up and the assessment of NEMO-eNATL60 simulations
 765 (Version v1). [available online at :<http://doi.org/10.5281/zenodo.4032732>].

766 Capó, E., Orfila, A., Mason, E., & Ruiz, S. (2019). Energy conversion routes in

- 767 the western mediterranean sea estimated from eddy–mean flow interactions. *J.*
768 *Phys. Oceanogr.*, *49*(1), 247–267.
- 769 Cessi, P. (2008). An energy-constrained parameterization of eddy buoyancy flux. *J.*
770 *Phys. Oceanogr.*, *38*(8), 1807–1819.
- 771 Chapron, B., Dérian, P., Mémin, E., & Resseguier, V. (2018). Large-scale flows un-
772 der location uncertainty: a consistent stochastic framework. *Quarterly Journal*
773 *of the Royal Meteorological Society*, *144*(710), 251–260.
- 774 Chen, R., Flierl, G. R., & Wunsch, C. (2014). A description of local and nonlo-
775 cal eddy–mean flow interaction in a global eddy-permitting state estimate. *J.*
776 *Phys. Oceanogr.*, *44*(9), 2336–2352.
- 777 Chen, R., Thompson, A. F., & Flierl, G. R. (2016). Time-dependent eddy-mean
778 energy diagrams and their application to the ocean. *J. Phys. Oceanogr.*, *46*(9),
779 2827–2850.
- 780 Davies, H. (1976). A lateral boundary formulation for multi-level prediction models.
781 *Q. J. R. Meteorolog. Soc.*, *102*(432), 405–418.
- 782 Dewar, W. K., & Bane, J. M. (1989). Gulf stream dynamics. part ii: Eddy energetics
783 at 73° w. *Journal of Physical Oceanography*, *19*(10), 1574–1587.
- 784 Ducet, N., & Le Traon, P.-Y. (2001). A comparison of surface eddy kinetic energy
785 and Reynolds stresses in the Gulf Stream and the Kuroshio Current systems
786 from merged TOPEX/Poseidon and ERS-1/2 altimetric data. *Journal of*
787 *Geophysical Research: Oceans*, *106*(C8), 16603–16622.
- 788 Eden, C., & Greatbatch, R. J. (2008). Towards a mesoscale eddy closure.
789 *Ocean Model.*, *20*(3), 223–239.
- 790 Engedahl, H. (1995). Use of the flow relaxation scheme in a three-dimensional baro-
791 clinic ocean model with realistic topography. *Tellus A*, *47*(3), 365–382.
- 792 Ferreira, D., Marshall, J., & Heimbach, P. (2005). Estimating eddy stresses by fit-
793 ting dynamics to observations using a residual-mean ocean circulation model
794 and its adjoint. *J. Phys. Oceanogr.*, *35*(10), 1891–1910.
- 795 Flather, R. A. (1994). A storm surge prediction model for the northern bay of ben-
796 gal with application to the cyclone disaster in april 1991. *J. Phys. Oceanogr.*,
797 *24*(1), 172–190.
- 798 Fox-Kemper, B., Ferrari, R., & Hallberg, R. (2008). Parameterization of mixed layer
799 eddies. part i: Theory and diagnosis. *J. Phys. Oceanogr.*, *38*(6), 1145–1165.

- 800 Gaspar, P., Grégoris, Y., & Lefevre, J.-M. (1990). A simple eddy kinetic energy
 801 model for simulations of the oceanic vertical mixing: Tests at station papa and
 802 long-term upper ocean study site. *Journal of Geophysical Research: Oceans*,
 803 *95*(C9), 16179–16193.
- 804 Gent, P. R., & McWilliams, J. C. (1990). Isopycnal mixing in ocean circulation
 805 models. *J. Phys. Oceanogr.*, *20*(1), 150–155.
- 806 Greatbatch, R. J., Zhai, X., Kohlmann, J.-D., & Czeschel, L. (2010). Ocean eddy
 807 momentum fluxes at the latitudes of the gulf stream and the kuroshio exten-
 808 sions as revealed by satellite data. *Ocean Model.*, *60*(3), 617–628.
- 809 Groeskamp, S., LaCasce, J. H., McDougall, T. J., & Rogé, M. (2020). Full-depth
 810 global estimates of ocean mesoscale eddy mixing from observations and theory.
 811 *Geophys. Res. Lett.*, *47*(18), e2020GL089425.
- 812 Grooms, I. (2017). Simulations of eddy kinetic energy transport in barotropic turbu-
 813 lence. *Physical Review Fluids*, *2*(11), 113801.
- 814 Grooms, I., Nadeau, L.-P., & Smith, K. S. (2013). Mesoscale eddy energy locality in
 815 an idealized ocean model. *J. Phys. Oceanogr.*, *43*(9), 1911–1923.
- 816 Hawkins, E., Smith, R. S., Gregory, J. M., & Stainforth, D. A. (2016). Irreducible
 817 uncertainty in near-term climate projections. *Clim. Dyn.*, *46*(11-12), 3807–
 818 3819.
- 819 Jamet, Q., Deremble, B., Wienders, N., Uchida, T., & Dewar, W. (2021). On Wind-
 820 driven Energetics of Subtropical Gyres. *Journal of Advances in Modeling Earth*
 821 *Systems*, e2020MS002329.
- 822 Jansen, M. F., Adcroft, A., Khani, S., & Kong, H. (2019). Toward an energetically
 823 consistent, resolution aware parameterization of ocean mesoscale eddies. *Jour-*
 824 *nal of Advances in Modeling Earth Systems*, *11*(8), 2844–2860.
- 825 Jouanno, J., Capet, X., Madec, G., Roullet, G., & Klein, P. (2016). Dissipation of
 826 the energy imparted by mid-latitude storms in the southern ocean. *Ocean Sci.*,
 827 *12*(3), 743–769.
- 828 Kang, D., & Curchitser, E. N. (2015). Energetics of eddy–mean flow interactions in
 829 the Gulf Stream region. *J. Phys. Oceanogr.*, *45*(4), 1103–1120.
- 830 Large, W. G., & Yeager, S. G. (2004). Diurnal to decadal global forcing for ocean
 831 and sea-ice models: the data sets and flux climatologies.
- 832 Leroux, S., Brankart, J.-M., Albert, A., Brodeau, L., Molines, J.-M., Jamet, Q.,

- 833 Le Sommer, J., Penduff, T., and Brasseur, P. (2021). Ensemble quantifica-
 834 tion of short-term predictability of the ocean fine-scale dynamics: A western
 835 mediterranean test-case at kilometric-scale resolution. *Manuscript submitted to*
 836 *Ocean Sci.*, $(-)$, $-$.
- 837 Madec, G., Bourdallé-Badie, R., Bouttier, P.-A., Bricaud, C., Bruciaferri, D.,
 838 Calvert, D., Chanut, J., Clementi, E., Coward, A., Delrosso, D., and others
 839 (2017). Nemo ocean engine.
- 840 Mak, J., Maddison, J. R., Marshall, D. P., & Munday, D. R. (2018). Implementa-
 841 tion of a geometrically informed and energetically constrained mesoscale eddy
 842 parameterization in an ocean circulation model. *J. Phys. Oceanogr.*, *48*(10),
 843 2363–2382.
- 844 Marshall, D. P., & Adcroft, A. J. (2010). Parameterization of ocean eddies:
 845 Potential vorticity mixing, energetics and arnold’s first stability theorem.
 846 *Ocean Model.*, *32*(3-4), 188–204.
- 847 Mellor, G. L., & Yamada, T. (1982). Development of a turbulence closure model for
 848 geophysical fluid problems. *Reviews of Geophysics*, *20*(4), 851–875.
- 849 Mémin, E. (2014). Fluid flow dynamics under location uncertainty. *Geophys. Astro-*
 850 *phys. Fluid Dynamics*, *108*(2), 119–146.
- 851 Millot, C. (1985). Some features of the algerian current. *Journal of Geophysical Re-*
 852 *search: Oceans*, *90*(C4), 7169–7176.
- 853 Millot, C. (1999). Circulation in the western mediterranean sea. *Journal of Marine*
 854 *Systems*, *20*(1-4), 423–442.
- 855 Obaton, D., Millot, C., d’Hières, G. C., & Taupier-Letage, I. (2000). The Algerian
 856 Current: Comparisons between in situ and laboratory data sets. *Deep Sea Re-*
 857 *search Part I: Oceanographic Research Papers*, *47*(11), 2159–2190.
- 858 Poulain, P.-M., Centurioni, L., Özgökmen, T., Tarry, D., Pascual, A., Ruiz, S.,
 859 Mauri, E., Menna, M., and Notarstefano, G. (2021). On the structure and
 860 kinematics of an algerian eddy in the southwestern mediterranean sea. *Remote*
 861 *Sensing*, *13*(15), 3039.
- 862 Renault, L., Molemaker, M. J., Gula, J., Masson, S., and McWilliams, J. C. (2016).
 863 Control and stabilization of the gulf stream by oceanic current interaction with
 864 the atmosphere. *J. Phys. Oceanogr.*, *46*(11), 3439–3453.
- 865 Renault, L., Molemaker, M. J., McWilliams, J. C., Shchepetkin, A. F., Lemarié,

- 866 F., Chelton, D., Illig, S., and Hall, A. (2016). Modulation of wind work by
 867 oceanic current interaction with the atmosphere. *J. Phys. Oceanogr.*, *46*(6),
 868 1685–1704.
- 869 Resseguier, V., Mémin, E., & Chapron, B. (2017). Geophysical flows under location
 870 uncertainty, part i random transport and general models. *Geophysical & Astro-*
 871 *physical Fluid Dynamics*, *111*(3), 149–176.
- 872 Roquet, F., Madec, G., McDougall, T. J., & Barker, P. M. (2015). Accurate poly-
 873 nomial expressions for the density and specific volume of seawater using the
 874 TEOS-10 standard. *Ocean Modelling*, *90*, 29–43.
- 875 Rossby, T. (1987). On the energetics of the gulf stream at 73w. *Journal of Marine*
 876 *Research*, *45*(1), 59–82.
- 877 Schubert, R., Gula, J., Greatbatch, R. J., Baschek, B., & Biastoch, A. (2020). The
 878 Submesoscale Kinetic Energy Cascade: Mesoscale Absorption of Submesoscale
 879 Mixed Layer Eddies and Frontal Downscale Fluxes. *J. Phys. Oceanogr.*, *50*(9),
 880 2573–2589.
- 881 Shchepetkin, A. F., & McWilliams, J. C. (2005). The regional oceanic modeling
 882 system (ROMS): a split-explicit, free-surface, topography-following-coordinate
 883 oceanic model. *Ocean modelling*, *9*(4), 347–404.
- 884 Stainforth, D. A., Allen, M. R., Tredger, E. R., & Smith, L. A. (2007). Confidence,
 885 uncertainty and decision-support relevance in climate predictions. *Philosophical*
 886 *Transactions of the Royal Society A: Mathematical, Physical and Engineering*
 887 *Sciences*, *365*(1857), 2145–2161.
- 888 Visbeck, M., Marshall, J., Haine, T., & Spall, M. (1997). Specification of eddy trans-
 889 fer coefficients in coarse-resolution ocean circulation models. *Journal of physical*
 890 *oceanography*, *27*(3), 381–402.
- 891 Waldman, R. (2016). *Etude multi-échelle de la convection océanique profonde en*
 892 *mer méditerranée: de l’observation à la modélisation climatique* (Unpublished
 893 doctoral dissertation). Université Paul Sabatier-Toulouse III.
- 894 Webster, F. (1961). The effect of meanders on the kinetic energy balance of the gulf
 895 stream. *Tellus*, *13*(3), 392–401.
- 896 Webster, F. (1965). Measurements of eddy fluxes of momentum in the surface layer
 897 of the gulf stream. *Tellus*, *17*(2), 240–245.
- 898 Wunsch, C., & Ferrari, R. (2004). Vertical mixing, energy, and the general circula-

tion of the oceans. *Annu. Rev. Fluid Mech.*, *36*, 281–314.